ACOUSTIC WAVE PROPAGATION IN A FLUID-FILLED BOREHOLE WITH A HORIZONTAL FRACTURE

by

X.M. Tang, C.H. Cheng, and M.N. Toksöz

Earth Resources Laboratory
Department of Earth, Atmospheric, and Planetary Sciences
Massachusetts Institute of Technology
Cambridge, MA 02139

ABSTRACT

The propagation of guided waves in a fluid-filled borehole with an open horizontal fracture is investigated both theoretically and experimentally. The fracture is modeled as a fluid layer that separates the domain of propagation into two regions. For the solution of the problem, we use a hybrid method to generate wave modes in the two regions. The modes are then summed to match the boundary conditions at the fracture surfaces. A singularity problem arises in matching the surface conditions and is regularized using a physical model based on the conservation of mass. Using the theory developed in this study, we study the transmission and reflection characteristics of borehole guided waves (i.e., Stoneley and pseudo-Rayleigh waves) due to the fracture. At low frequencies, the effects of a fracture on the Stoneley wave are dominated by the fluid flow into the fracture. As frequency increases, mode conversion at the fracture becomes significant. Above the cut-off frequency of the pseudo-Rayleigh wave, part of the incident Stoneley wave is converted to pseudo-Rayleigh waves, which is demonstrated by synthetic microseismograms. The pseudo-Rayleigh wave is substantially affected by the fracture. Because this wave requires the formation shear strength to sustain its propagation, even a thin fracture with zero shear strength can significantly attenuate the wave amplitude and produce strong reflection. This effect is more pronounced towards the cut-off frequencies than away from the frequencies. Consequently, the lack of pseudo-Rayleigh energy across a fracture may be used as a sensitive indicator in fracture detection and characterization.

Ultrasonic experiments have been performed to measure the transmission of guided waves across laboratory borehole fracture models. For the Stoneley waves, we performed the experiment below the cut-off frequency of the pseudo-Rayleigh wave and the experimental results are in good agreement with the theory. For the pseudo-Rayleigh wave, we performed the experiment in a higher frequency range. The experiment has verified the substantial effects of a fracture on this wave mode. The weak early arrivals

of the transmitted waves have also been observed for thin as well as thick fractures. This confirms the theoretical prediction that the transmission of the pseudo-Rayleigh wave is the smallest towards the cut-off frequencies. The measured transmission coefficients agree with theoretical results.

In summary, we have presented an analysis on the guided wave propagation across a borehole horizontal fracture. The wave characteristics in the vicinity of a fracture as described in this study may be used to provide useful information for the detection and characterization of borehole fractures using acoustic logging techniques.

INTRODUCTION

The characterization of borehole fractures is important in reservoir evaluation and hydrocarbon production. Full waveform acoustic logs provide a means of fracture detection and characterization. Field measurements have shown effects of permeable fractures on the attenuation of borehole acoustic waves (Paillet, 1980; Hsu et al., 1985; Hardin et al., 1987; Brie et al., 1988). Borehole Stoneley (or tube) waves have been of special interest because these waves dominate the low frequency portion of the acoustic logs. Tang et al. (1989) have studied the effects of a vertical borehole fracture on the Stoneley propagation, and shown that the major effects are the Stoneley attenuation due to fluid flow into the fracture. In the present study, we will treat the problem of borehole guided wave propagation across a horizontal fracture. Because this is such an important and interesting problem, it has been treated by several authors using finite-difference modeling (Stephen, 1986; Stephen et al., 1985; Bhashvanija, 1983). These calculations require large fracture apertures in the modeling because of the number of nodal points needed to resolve effects of the fracture. In addition, although these calculations display the wave characteristics in the vicinity of the fracture, the response of each individual wave component, such as pseudo-Rayleigh or Stoneley mode, to the fracture is not easy to resolve because of the overlap of the waveforms in the time domain. Therefore, the major purpose of this study is to analyze the effects of fractures with different apertures on the borehole guided waves. The results are expected to provide useful information for fracture detection and characterization using acoustic logging techniques.

The borehole guided waves, or Stoneley and pseudo-Rayleigh waves, are the dominant waves on an acoustic log. Their response to the effects of a fracture will be easily recognized in terms of changes in the wave amplitude. In the presence of a horizontal fracture, the problem becomes more complicated than the case of a vertical fracture because, in addition to the fluid flow into the fracture, the scattering effects of the fracture should also be considered. A borehole guided wave is coupled with the wave motion in the formation. This coupling will be affected when the formation wave energy encounters a discontinuity (the fracture). For the fluid flow effects, Tang and

Cheng (1989) and Hornby et al. (1989) have developed similar dynamic flow models to account for the Stoneley attenuation due to these effects. In this study, we will extend the treatment to incorporate scattering effects of the fracture by matching the boundary conditions at the fracture surfaces. We will also extend the treatment to pseudo-Rayleigh waves.

The present problem involves treating a discontinuity that intersects the direction of borehole wave propagation. Because of the discontinuity, the problem cannot be solved using the conventional wavenumber integration technique (Cheng et al., 1981). The difficulty lies in the necessity that the solutions must satisfy conditions at two perpendicular boundaries, i.e., the borehole boundary and the fracture surfaces. However, if modal solutions for the borehole propagation are used, the boundary conditions at the borehole boundary are automatically satisfied and one can use the sum of the modes to match boundary conditions at the fracture surfaces. Although the combination of the borehole leaking modes can be used for this purpose, the multivaluedness of these modal functions will force one to perform integrations along contours on the complex frequency and wavenumber planes (Haddon, 1987, 1989), which is inconvenient for the present problem where boundary conditions at the fracture are matched for each real frequency. In this study, we adopt a hybrid method used by Tsang (1985, 1987) and Nolet et al. (1989). We introduce an artificial boundary at a radial distance that is large compared to the borehole radius. This boundary generates discrete wave modes, which form a basis for the solutions in the regions separated by the fracture. Boundary conditions at the fracture surfaces then couple the solutions in the two regions. This coupling results in the transmission and reflection of the incident borehole acoustic waves.

THEORETICAL FORMULATION

Let us consider the borehole and fracture configuration shown in Figure 1. The fracture is modeled as a horizontal fluid layer with thickness L, which crosses the borehole perpendicularly. The fracture separates the domain of propagation into two regions. If taking the borehole as z, the upper region is the $z < 0$ region, while the lower one is the $z > L$ region. The formation for the two regions is an isotropic homogeneous elastic solid, with compressional and shear velocities V_p and V_s, and density ρ. The borehole and the fracture are filled with the same fluid having acoustic velocity V_f and density ρ_f. In either the upper or lower region, the borehole fluid displacement potential ϕ_f and the formation compressional and shear displacement potentials ϕ_s and ψ_s satisfy the following wave equations:

$$\begin{aligned} \nabla^2\phi_f + k_f^2\phi_f &= 0 \ , \\ \nabla^2\phi_s + k_p^2\phi_s &= 0 \ , \end{aligned} \tag{1}$$

$$\nabla^2\psi_s + k_s^2\psi_s = 0 \ .$$

where $\nabla^2 = \frac{\partial^2}{\partial r^2} + \frac{1}{r}\frac{\partial}{\partial r} + \frac{\partial^2}{\partial z^2}$ is the cylindrical Laplace operator, r is the radial variable, $k_f = \omega/V_f$, $k_p = \omega/V_p$, $k_s = \omega/V_s$, and ω is the angular frequency. In this problem, the azimuthal symmetry is assumed. From the potentials, the fluid and formation displacement vectors $\vec{u}_f$ and $\vec{u}_s$ are calculated using

$$\begin{aligned} \vec{u}_f &= \nabla\phi_f \\ \vec{u}_s &= \nabla\phi_s + \nabla\times(\psi_s\vec{e}_z) \end{aligned} \tag{2}$$

where $\vec{e}_z$ is the unit vector along z axis. In the frequency domain, the fluid stresses are simply

$$\sigma_{rrf} = \sigma_{zzf} = -\rho_f\omega^2\phi_f \ , \tag{3}$$

and the formation stress components are calculated using

$$\begin{aligned} \sigma_{rrs} &= \lambda[\frac{1}{r}\frac{\partial}{\partial r}(ru_{rs}) + \frac{\partial u_{zs}}{\partial z}] + 2\mu\frac{\partial u_{rs}}{\partial r} \ , \\ \sigma_{zzs} &= \lambda[\frac{1}{r}\frac{\partial}{\partial r}(ru_{rs}) + \frac{\partial u_{zs}}{\partial z}] + 2\mu\frac{\partial u_{zs}}{\partial z} \ , \\ \sigma_{rzs} &= \mu(\frac{\partial u_{rs}}{\partial z} + \frac{\partial u_{zs}}{\partial r}) \ , \end{aligned} \tag{4}$$

where λ and μ are Lamé constants of the formation and can be calculated from the given V_p, V_s, and ρ of the formation.

Construction of Modal Solutions

In order to generate modal solutions for the problem, we place an artificial boundary at $r = d$ ($d \gg a$). At this boundary, we let the displacement components u_{rs} and u_{zs} vanish so that it represents a rigid boundary. At the borehole boundary $r = a$, we have the continuity of the normal stress and radial displacement, and the vanishing of the formation shear stress. With the given radial boundaries, the solutions to Eqs. (1) can be written as

$$\begin{aligned} \phi_f &= AI_0(fr)exp(ikz) \ , \\ \phi_s &= [BK_0(lr) + B'I_0(lr)]exp(ikz) \ , \\ \psi_s &= [CK_1(mr) + C'I_1(mr)]exp(ikz) \ . \end{aligned} \tag{5}$$

with

$$f = \sqrt{k^2 - k_f^2} \ , \quad l = \sqrt{k^2 - k_p^2} \ , \quad m = \sqrt{k^2 - k_s^2} \ , \tag{6}$$

where k is the axial wave number, I_n and K_n ($n = 0, 1$) are the first and second kind modified Bessel functions of order n, respectively, and A, B, B', C, and C' are constants to be determined. From the potentials in Eqs. (5), the stress and displacement

components can be calculated using Eqs. (2), (3), and (4). They are given in Appendix A. Upon using the boundary conditions at $r = a$ and $r = d$, a system of equations for determining the constants in Eqs. (5) is obtained as follows

$$\begin{bmatrix} a_{11} & a_{12} & a_{13} & a_{14} & a_{15} \\ a_{21} & a_{22} & a_{23} & a_{24} & a_{25} \\ 0 & a_{32} & a_{33} & a_{34} & a_{35} \\ 0 & a_{42} & a_{43} & a_{44} & a_{45} \\ 0 & a_{52} & a_{53} & a_{54} & a_{55} \end{bmatrix} \begin{bmatrix} A \\ B \\ B' \\ C \\ C' \end{bmatrix} = 0 \tag{7}$$

where the matrix elements a_{ij} are given in Appendix B. The condition that there be nontrivial solutions for A, B, B', C, and C' requires that the determinant of Eq. (7) (denoted by D) vanish. This leads to

$$D(k,\omega) = 0 \ . \tag{8}$$

For a given frequency ω, Eq. (8) determines M number of values for k, denoted by k_α ($\alpha = 1, 2, \cdots, M$). Each k_α is associated with a wave mode. As already shown by Tsang (1987), for real ω these k values are located at the real and imaginary k axes. The mode with $k_\alpha > k_f$ is the well known Stoneley wave; the modes with $k_s > k_\alpha > k_f$ are the pseudo-Rayleigh modes. The Stoneley and pseudo-Rayleigh are guided waves that are trapped in the borehole and are therefore insensitive to the boundary at $r = d$ if $d \gg a$. The modes with $Re\{k_\alpha\} < k_s$ are radiation modes. The fact that their locations coincide with the Sommerfeld branch cut indicates that the mode locations represent the discretization of the branch cut, and the sum of the modes approximates the contribution from this cut (Tsang, 1987). Therefore, the total modes form a basis for the solution to the borehole wave motion. The wave motion of each mode is distributed both in the borehole and in the formation, as shown in Eqs. (5). The constants in Eqs. (5) govern this distribution. After k_α is evaluated, the normalized eigenvector for the constants is found by solving Eq. (7) with A set to 1. The αth eigenvector is denoted by [1, B_α, B'_α, C_α, C'_α].

It is worthwhile to mention some of the numerical manipulations that are required to calculate the roots of Eq. (8) and their associated eigenvectors. Because the radial boundary $r = d$ is a large number, the Bessel functions I_n ($n = 0, 1$) evaluated at this boundary may create overflow problems. To overcome this difficulty, we make the following substitutions:

$$\begin{aligned} B'' &= B' I_0(ld) \qquad \text{if } k > k_p \\ C'' &= C' I_0(md) \qquad \text{if } k > k_s \end{aligned} \tag{9}$$

When Eqs.(9) are used, the the fourth and fifth columns of the matrix in Eq. (7) are modified as:

$$\begin{aligned} a_{i4} &\rightarrow a_{i4}/I_0(ld) \ , \ \text{if } k > k_p \ , \\ a_{i5} &\rightarrow a_{i5}/I_0(md) \ , \ \text{if } k > k_s \ , \end{aligned}$$

where i =1,2,3,4,and 5. Once B'' and C'' are found from the modified Eq. (7), Eqs. (9) are used to recover B' and C'. The overflow problem is thus overcome.

Another manipulation is in the root finding procedure of Eq. (8). The modes are generally close together around k_p and k_s (Tsang, 1987). This behavior poses some difficulty in locating these modes. It is therefore advisable to locate the modes using l instead of k when k is around k_p, and using m when k is around k_s. This can be seen by noting a relation that can be derived from Eqs. (6), i.e., $dl = kdk/\sqrt{k^2 - k_p^2}$; when k is close to k_p, the separation dl on the l axis is much bigger than dk on the k axis. The same is true for dm.

It has been proved that the modes so determined satisfy the following orthogonality relation (Tsang, 1987)

$$\int_0^a \sigma_{zzf}(k_\beta, r)u_{zf}(k_\alpha, r)rdr + \int_a^d [\sigma_{zzs}(k_\beta, r)u_{zs}(k_\alpha, r) - \sigma_{rzs}(k_\alpha, r)u_{rs}(k_\beta, r)]rdr = W(k_\beta)\delta_{\alpha\beta} \ , \tag{10}$$

where $\delta_{\alpha\beta}$ is the Kronecker delta, and the normalization constant $W(k_\alpha)$ is given by (Tsang, 1987)

$$W(k_\alpha) = -\frac{i\rho_f\omega^2}{2}\frac{(\partial D/\partial k_\alpha)(\omega, k_\alpha)}{N(\omega, k_\alpha)} \ , \tag{11}$$

where $N(\omega, k_\alpha)$ is the determinant of a 5×5 matrix. This matrix is obtained from the one in Eq. (7) by replacing a_{11} with $-k_f^2 K_0(fa)$ and a_{21} with $fK_1(fa)$, respectively. Eq. (11) can be readily derived from the evaluation of the mode amplitude using the theorem of residues (see Tsang, 1987). The factor $-i\rho_f\omega^2/2$ in Eq. (11) was given as $-\rho_f\omega^2/\pi$ in Tsang's (1987) Eq. (9). This is because he used Hankel and Bessel functions, and here we use modified Bessel functions. The orthogonality equation given in Eq. (10) is an important relation that will later be used to determine the mode coupling at the fracture surfaces.

Solution of Wave Motion in the Fracture Fluid Layer

The solution for the fracture fluid wave motion is needed in order to couple the wave motions in the two regions separated by the fracture. The fracture fluid displacement potential ϕ satisfies the wave equation

$$\frac{1}{r}\frac{\partial}{\partial r}(r\frac{\partial \phi}{\partial r}) + \frac{\partial^2 \phi}{\partial z^2} + k_f^2\phi = 0 \ , \ 0 < r < d, 0 < z < L \ . \tag{12}$$

In terms of ϕ, the fluid displacement $\vec{u}$ and pressure p are given by

$$\begin{aligned} \vec{u} &= \nabla\phi \ , \\ p &= \rho_f\omega^2\phi \ . \end{aligned} \tag{13}$$

At $r = d$, we let the fluid motion satisfy the same rigid boundary condition as in either the upper or lower region, i.e.,

$$\frac{\partial \phi}{\partial r} = 0 \ , \ \text{at } r = d \ . \tag{14}$$

At the fracture surfaces $z = 0$ and $z = L$, we prescribe the values of ϕ, which are related to the normal stresses σ_{zzf} and σ_{zzs} of the two regions through the continuity of these stresses. To find the solution of Eq. (12) with the given boundary conditions, we first solve the Green's function determined by the following boundary value problem.

$$\begin{cases} \frac{1}{r}\frac{\partial}{\partial r}(r\frac{\partial G}{\partial r}) + \frac{1}{r^2}\frac{\partial^2 G}{\partial \theta^2} + \frac{\partial^2 G}{\partial z^2} + k_f^2 G = -\frac{4\pi}{r}\delta(r - r_0)\delta(\theta - \theta_0)\delta(z - z_0) \\ G = 0 \ \text{ at } z = 0 \text{ and } L \ ; \ \frac{\partial G}{\partial r} = 0 \ \text{ at } r = d \ , \end{cases} \tag{15}$$

where θ is the azimuthal variable, (r_0, θ_0, z_0) and (r, θ, z) are source and field points, respectively, and δ is the Dirac delta function. Following the procedures for finding Green's function (Morse and Feshbach, 1953), the solution to Eq. (15) is found to be

$$G(r, \theta, z, \omega; r_0, \theta_0, z_0) =$$
$$\frac{4}{d^2} \sum_{m,n} \frac{e^{im(\theta - \theta_0)} J_m(\zeta_{mn} r) J_m(\zeta_{mn} r_0)}{(1 - \frac{m^2}{\zeta_{mn}^2}) J_m^2(\zeta_{mn} d)} \frac{\sinh(\sqrt{\zeta_{mn}^2 - k_f^2}\ z_<) \sinh[\sqrt{\zeta_{mn}^2 - k_f^2}(L - z_>)]}{\sqrt{\zeta_{mn}^2 - k_f^2}\ \sinh(\sqrt{\zeta_{mn}^2 - k_f^2} L)} \ , \tag{16}$$

where

$$z_< = min(z, z_0) \ , \text{ and } \ z_> = max(z, z_0) \ ,$$

the symbol sinh represents the hyperbolic function, and $\zeta_{mn} d$ is the nth root of

$$J_m'(\zeta_{mn} d) = 0 \ , \ \ n = 1, 2, 3, \cdots \tag{17}$$

By using Green's theorem, ϕ is expressed as

$$\phi = \frac{1}{4\pi} \iint_{S_0} (G \frac{\partial \phi}{\partial n_0} - \phi \frac{\partial G}{\partial n_0}) dS_0 \ , \tag{18}$$

where n_0 is the outward normal to the boundary surface S_0, which now includes the upper and lower surfaces of the fluid layer, as well as the circular strip at $r = d$. Using the respective boundary conditions for ϕ and G at $z = 0$ and L, and $r = d$, we can express ϕ using the surface integrals over the upper and lower surfaces of the fracture fluid layer.

$$\phi = \frac{1}{4\pi} \iint_{z_0 = 0} \phi \frac{\partial G}{\partial z_0} dS_0 - \frac{1}{4\pi} \iint_{z_0 = L} \phi \frac{\partial G}{\partial z_0} dS_0 \tag{19}$$

Because of the azimuthal symmetry in ϕ and the orthogonality of the function $exp(im\theta_0)$ over the interval $[0, 2\pi]$, the integration over S_0 knocks out all the $m \neq 0$ terms in the Green's function given in Eq. (16). Thus we only need to use the $m = 0$ terms of this equation. In addition, for $m = 0$, Eq. (17) becomes

$$J_1(\zeta_n d) = 0 \ , \quad n = 1, 2, 3 \cdots \tag{20}$$

The summation in Eq. (16) is now over the positive roots (including $\zeta d = 0$) of Eq. (20). In the following, Eq. (19) will be used to couple the wave motions at both sides of the fracture.

Determination of Transmission and Reflection of Incident Waves

We now let a borehole wave be incident on the fracture and determine its transmission and reflection. In the $z < 0$ region there are incident and reflected waves, while in the $z > L$ region, there are only transmitted waves. The reflected waves propagate in negative z direction and have $exp(-ik_\alpha z)$ dependencies. It has been shown (Tsang, 1987) that replacing k_α with $-k_\alpha$ will not change the sign of σ_{zzs}, σ_{zzf}, and u_{rs} but will reverse the sign of u_{zf}, u_{zs}, and σ_{rzs}. In the following, this property will be used to write the boundary conditions at the $z = 0$ surface. At this surface, we have the continuity of normal stress and displacement, and the vanishing of shear stress. In the $z < 0$ region, these quantities are expressed by the linear combination of the incident and reflected modes, while in the fracture fluid layer the pressure and displacement are derived from Eqs. (13) and (19). We therefore have the following equations for the $z = 0$ surface:
For $0 < r \leq a$

$$\sum_\alpha (b_\alpha^+ - b_\alpha^-) u_{zf}(k_\alpha, r) = \frac{\partial \phi}{\partial z} \ , \tag{21}$$

$$\sum_\alpha (b_\alpha^+ + b_\alpha^-) \sigma_{zzf}(k_\alpha, r) = -\rho_f \omega^2 \phi \ . \tag{22}$$

For $a < r \leq d$

$$\sum_\alpha (b_\alpha^+ - b_\alpha^-) u_{zs}(k_\alpha, r) = \frac{\partial \phi}{\partial z} \ , \tag{23}$$

$$\sum_\alpha (b_\alpha^+ + b_\alpha^-) \sigma_{zzs}(k_\alpha, r) = -\rho_f \omega^2 \phi \ , \tag{24}$$

$$\sum_\alpha (b_\alpha^+ - b_\alpha^-) \sigma_{rzs}(k_\alpha, r) = 0 \ , \tag{25}$$

where b_α^+ and b_α^- are amplitude coefficients of the αth incident and reflected wave modes, respectively. We then make use of the orthogonality relation (Eq. 10) to relate

these equations. Multiply Eq. (21) by $\sigma_{zzf}(k_\beta, r)r$ and integrate from 0 to a. Next, multiply Eq. (23) by $\sigma_{zzs}(k_\beta, r)r$ and Eq. (25) by $-u(k_\beta, r)r$ and integrate from a to d. Add the equations together and apply Eq. (10) to the left hand side of the resulting equation. We obtain

$$W(k_\beta)(b_\beta^+ - b_\beta^-) = \int_0^d \sigma_{zz}(k_\beta, r) \left.\frac{\partial \phi}{\partial z}\right|_{z=0} r dr \ , \tag{26}$$

where the normal stress σ_{zz} equals σ_{zzs} in the formation and σ_{zzf} in the borehole. Similarly, we match boundary conditions at the lower boundary $z = L$ using the transmitted wave modes and Eq. (19).
For $0 < r \leq a$

$$\sum_\alpha c_\alpha^+ u_{zf}(k_\alpha, r) = \frac{\partial \phi}{\partial z} \ , \tag{27}$$

$$\sum_\alpha c_\alpha^+ \sigma_{zzf}(k_\alpha, r) = -\rho_f \omega^2 \phi \ . \tag{28}$$

For $a < r \leq d$

$$\sum_\alpha c_\alpha^+ u_{zs}(k_\alpha, r) = \frac{\partial \phi}{\partial z} \ , \tag{29}$$

$$\sum_\alpha c_\alpha^+ \sigma_{zzs}(k_\alpha, r) = -\rho_f \omega^2 \phi \ , \tag{30}$$

$$\sum_\alpha c_\alpha^+ \sigma_{rzs}(k_\alpha, r) = 0 \ , \tag{31}$$

where c_α^+ is the amplitude coefficient of the αth transmitted wave mode. In Eqs. (27) through (31), a factor $exp(ik_\alpha L)$ is absorbed in c_α^+ because these equations are evaluated at the $z = L$ surface. Again, following the same procedure as for the upper boundary $z = 0$, we obtain

$$W(k_\beta)c_\beta^+ = \int_0^d \sigma_{zz}(k_\beta, r) \left.\frac{\partial \phi}{\partial z}\right|_{z=L} r dr \ . \tag{32}$$

To get $\frac{\partial \phi}{\partial z}$ needed in Eqs. (26) and (32), we differentiate Eq. (19) with respect to z. This results in

$$\frac{\partial \phi}{\partial z} = \frac{1}{4\pi} \iint_{z_0=0} \phi \frac{\partial^2 G}{\partial z \partial z_0} dS_0 - \frac{1}{4\pi} \iint_{z_0=L} \phi \frac{\partial^2 G}{\partial z \partial z_0} dS_0 \ . \tag{33}$$

At this stage, mathematical difficulty arises when we let $z \to 0$ and $z \to L$ to obtain the surface values of $\frac{\partial \phi}{\partial z}$. This is because the kernel of the integrals $\frac{\partial^2 G}{\partial z \partial z_0}$ is strongly singular in view of the discontinuity in G as a function of the field point, when the

source point is on the boundary surface (Morse and Feshbach, 1953). The integrals are therefore non-integrable in the classical sense. Nevertheless, multiplying equations like Eq. (33) by a regularizing function and integrating over the field points may regularize this kind of problem (Delves and Walsh, 1974), providing that this function has good behavior over the domain of integration. In the present case, the regularizing function is $\sigma_{zz}(k_\beta, r)$ in Eqs. (26) and (32). However, the integrals in these two equations are still singular because σ_{zz} is discontinuous at $r = a$ [$\sigma_{zzf}(k,a) \neq \sigma_{zzs}(k,a)$]. We therefore define a continuous stress function

$$\sigma^1_{zz}(k_\beta, r) = \begin{cases} \sigma_{zzs}(k_\beta, r) & a < r \leq d \\ \sigma_{zzf}(k_\beta, r) + [\sigma_{zz}(k_\beta, a)]H(a-r) & 0 < r \leq a \end{cases} \tag{34}$$

where $[\sigma_{zz}(k,a)] = \sigma_{zzs}(k,a) - \sigma_{zzf}(k,a)$ is the normal stress discontinuity at the borehole boundary $r = a$ and $H(a-r)$ is the step function. By using σ^1_{zz}, the integrals in Eqs. (26) and (32) become

$$\int_0^d \sigma_{zz}(k_\beta, r)\frac{\partial \phi}{\partial z} r dr = \int_0^d \sigma^1_{zz}(k_\beta, r)\frac{\partial \phi}{\partial z} r dr - [\sigma_{zz}(k_\beta, a)] \int_0^a \frac{\partial \phi}{\partial z} r dr \ . \tag{35}$$

Because the discontinuity is removed from σ^1_{zz}, the first term of Eq. (35) is now regular. By substituting $\phi|_{z_0=0}$ given in Eqs. (22) and (24) and $\phi|_{z_0=L}$ in Eqs. (28) and (30) into Eq. (33), this term, evaluated at $z = 0$ and L, may now be respectively written as

$$\begin{aligned} \textstyle\int_0^d \sigma^1_{zz}(k_\beta, r)\frac{\partial \phi}{\partial z}\Big|_{z=0} r dr &= \textstyle\sum_\alpha (b^+_\alpha + b^-_\alpha)\Theta_{\alpha\beta} - \sum_\alpha c^+_\alpha \Theta'_{\alpha\beta} \ , \\ \textstyle\int_0^d \sigma^1_{zz}(k_\beta, r)\frac{\partial \phi}{\partial z}\Big|_{z=L} r dr &= \textstyle\sum_\alpha (b^+_\alpha + b^-_\alpha)\Theta'_{\alpha\beta} - \sum_\alpha c^+_\alpha \Theta_{\alpha\beta} \ , \end{aligned} \tag{36}$$

with

$$\begin{pmatrix} \Theta_{\alpha\beta} \\ \Theta'_{\alpha\beta} \end{pmatrix} = \frac{2}{d^2 \rho_f \omega^2} \sum_{\zeta_n} \frac{I(k_\alpha, \zeta_n) I_1(k_\beta, \zeta_n)}{J_0^2(\zeta_n d)} \frac{\sqrt{\zeta_n^2 - k_f^2}}{\sinh(\sqrt{\zeta_n^2 - k_f^2}\, L)} \begin{pmatrix} \cosh(\sqrt{\zeta_n^2 - k_f^2}\, L) \\ 1 \end{pmatrix} , \tag{37}$$

where the summation in Eqs. (37) is over the roots of Eq. (20) and

$$I(k_\alpha, \zeta_n) = \int_0^d \sigma_{zz}(k_\alpha, r) J_0(\zeta_n r) r dr \tag{38}$$

$$I_1(k_\beta, \zeta_n) = \int_0^d \sigma^1_{zz}(k_\beta, r) J_0(\zeta_n r) r dr \tag{39}$$

can be analytically integrated out and are listed in Appendix C. The second term in Eq. (35) carries the singularity of the problem (using Eqs. (16) and (33), one can show that this term is divergent). Since the integration of this term is over the borehole area, we can regularize it using a physical model based on the conservation of mass. From

Eqs. (13), we see that $\left.\frac{\partial\phi}{\partial z}\right|_{z=L}$ is the axial borehole fluid displacement at the lower boundary $z = L$. Multiplying this term by $-i\omega$ and integrating over the borehole area gives the borehole fluid flux through the boundary. Based on the conservation of mass, the difference between the flux through the $z = L$ boundary and that through the $z = 0$ boundary equals the fluid flux into the fracture. Thus we have

$$-i\omega 2\pi \int_0^a \left.\frac{\partial\phi}{\partial z}\right|_{z=L} r dr + i\omega 2\pi \int_0^a \left.\frac{\partial\phi}{\partial z}\right|_{z=0} r dr = 2\pi a q \ , \tag{40}$$

where q is the volume flow rate per unit fracture length. According to the theory of dynamic conductivity of an open fracture (Tang and Cheng, 1989), q is given by

$$q = -\bar{C}\frac{\partial p}{\partial r} \ , r = a \tag{41}$$

where $\bar{C}$ is the fracture dynamic conductivity and $\frac{\partial p}{\partial r}$ is the dynamic pressure gradient at the fracture opening. If we assume that the viscous skin depth of the fluid is small compared to the fracture aperture L, $\bar{C}$ is then given by (Tang and Cheng, 1989)

$$\bar{C} = \frac{iL}{\omega\rho_f} \ . \tag{42}$$

In addition, we assume that the fluid flux into the fracture is mainly carried away by the fracture fundamental wave mode as in the case of a vertical fracture (see Tang et al., 1989). Then the pressure associated with this wave is given by the Hankel function $p_0 H_0^{(1)}(k_{fr} r)$, where p_0 is the pressure at the fracture opening and the fracture wavenumber k_{fr} is found by solving the fracture wave dispersion equation for the fundamental mode (Tang et al., 1989). The pressure gradient at the fracture opening is obtained as

$$\frac{\partial p}{\partial r} = -p_0 k_{fr} \frac{H_1^{(1)}(k_{fr} a)}{H_0^{(1)}(k_{fr} a)} \ . \tag{43}$$

We assume that p_0 is the average of the borehole pressures of the upper and lower surfaces evaluated at $r = a$. Using Eqs. (22) and (28), we have

$$p_0 = \frac{1}{2}\rho_f \omega^2 (\phi|_{z=0} + \phi|_{z=L})|_{r=a} = -\frac{1}{2}\sum_\alpha (b_\alpha^+ + b_\alpha^- + c_\alpha^+)\sigma_{zzf}(k_\alpha, a) \ . \tag{44}$$

With q determined, Eq. (40) is then used to regularize the second term of Eq. (35). To couple the fluid flow at $z = 0$ and $z = L$, we express the flux through $z = 0$ using q and the flux through $z = L$. The latter flux is calculated with $\left.\frac{\partial\phi}{\partial z}\right|_{z=L}$ given in Eq. (21). Similarly, we express the flux through $z = L$ using q and the flux through $z = 0$. The latter flux is calculated using the surface value of $\left.\frac{\partial\phi}{\partial z}\right|_{z=0}$ given in Eq. (27).

Finally, we obtain the following coupled matrix equations for vectors $\mathbf{b}^-$ and $\mathbf{c}^+$, which respectively contain the reflected and transmitted amplitude coefficients.

$$\begin{aligned} \mathbf{W}(\mathbf{b}^+ - \mathbf{b}^-) &= \mathbf{\Theta}(\mathbf{b}^+ + \mathbf{b}^-) - \mathbf{\Theta}'\mathbf{c}^+ + \mathbf{N}(\mathbf{b}^+ + \mathbf{b}^- + \mathbf{c}^+) + \mathbf{K}\mathbf{c}^+ \\ \mathbf{W}\mathbf{c}^+ &= \mathbf{\Theta}'(\mathbf{b}^+ + \mathbf{b}^-) - \mathbf{\Theta}\mathbf{c}^+ - \mathbf{N}(\mathbf{b}^+ + \mathbf{b}^- + \mathbf{c}^+) - \mathbf{K}(\mathbf{b}^+ - \mathbf{b}^-) \end{aligned} \tag{45}$$

where $\mathbf{W}$ is a diagonal matrix with the $\beta\beta$ element equal to $W(k_\beta)$, $\mathbf{\Theta}$ and $\mathbf{\Theta}'$ have been defined in Eqs. (37), and $\mathbf{K}$ and $\mathbf{N}$ are $M \times M$ square matrices whose elements are as follows

$$\begin{aligned} K_{\alpha\beta} &= \frac{ik_\alpha a}{f_\alpha} I_1(f_\alpha a)[\sigma_{zz}(k_\beta, a)] \\ N_{\alpha\beta} &= \frac{aL}{2} I_0(f_\alpha a) k_{fr} \frac{H_1^{(1)}(k_{fr}a)}{H_0^{(1)}(k_{fr}a)} [\sigma_{zz}(k_\beta, a)] \end{aligned} \tag{46}$$

where f_α is calculated by replacing k in f given in Eqs. (6) with k_α. To solve the coupled matrix equations (Eqs. 45), we use the auxiliary vectors

$$\begin{aligned} \mathbf{x} &= (\mathbf{b}^- + \mathbf{c}^+)/\mathbf{2} \\ \mathbf{y} &= (\mathbf{b}^- - \mathbf{c}^+)/\mathbf{2} \end{aligned} \tag{47}$$

and obtain the following decoupled matrix equations for $\mathbf{x}$ and $\mathbf{y}$, respectively.

$$\begin{aligned} (\mathbf{W} - \mathbf{\Theta} - \mathbf{\Theta}' + \mathbf{K})\mathbf{b}^+ &= (\mathbf{W} + \mathbf{\Theta} + \mathbf{\Theta}' + \mathbf{K})\mathbf{x} \\ (\mathbf{W} - \mathbf{\Theta} + \mathbf{\Theta}' - \mathbf{K} - \mathbf{2N})\mathbf{b}^+ &= (\mathbf{W} + \mathbf{\Theta} - \mathbf{\Theta}' - \mathbf{K} + \mathbf{2N})\mathbf{y} \end{aligned} \tag{48}$$

Once $\mathbf{x}$ and $\mathbf{y}$ are found by independently solving the above equations, the vectors $\mathbf{b}^-$ and $\mathbf{c}^+$ are obtained using Eqs. (47), and the transmission and reflection of the incident wave are thus determined.

We now give a short discussion on the present theory and its relevance to previous models. In the above theoretical development, we balance the fluid flow across and into the fracture in order to overcome the singularity problem. This technique has been used by Tang and Cheng (1989) and Hornby et al. (1989) in their modeling of Stoneley attenuation across a fracture. In keeping with the fluid flow feature of the previous models, the present theory includes effects of mode conversion at the fracture by matching the boundary condition at fracture surfaces. Thus we expect that there are similarities and differences between the present model and previous models. In addition, the balance of fluid flow is appropriate for the incidence of guided waves that are trapped in the borehole, since these waves can produce an effective borehole pressure to drive the flow into the fracture. However, the radiation modes are oscillatory across the borehole and their energy is largely distributed in the formation. Thus the balance of flow may not be applicable to the incidence of these modes. Therefore, we will only determine the transmission and reflection for the guided wave incidence, which is the major interest of this study.

Let a guided wave mode with amplitude coefficient b_α^+ be incident on the fracture, we can calculate the resulting transmitted and reflected amplitude coefficients c_α^+ and

b_α^- corresponding to the same mode (Stoneley or pseudo-Rayleigh). This defines the transmission and reflection coefficients of this wave mode.

$$\begin{aligned} T_{rs} &= c_\alpha^+ / b_\alpha^+ \ , \\ R_{fl} &= b_\alpha^- / b_\alpha^+ \ , \end{aligned} \tag{49}$$

where the subscript α refers to either Stoneley or pseudo-Rayleigh wave mode.

Synthetic Microseismograms

Given a guided wave mode generated at a distance h above the fracture in the region I, we let this mode be incident on the fracture. At the source, the amplitude coefficient is $1/W(k_{in})$ (Tsang, 1987), where k_{in} is the wavenumber of the incident mode. At the upper fracture surface, this coefficient becomes

$$b_{in}^+ = \frac{e^{ik_{in}h}}{W(k_{in})} \ . \tag{50}$$

Upon interacting with the fracture, the incident wave energy is partly reflected and partly transmitted, together with some converted wave energy originating from the fracture. Thus in region I, the total borehole fluid pressure wave field is

$$P^I = \rho_f \omega^2 [b_{in}^+ \phi_f(k_{in}, r) e^{ik_{in}z} + \sum_\alpha b_\alpha^- \phi_f(k_\alpha, r) e^{-ik_\alpha z}] \ , \quad z < 0 \ . \tag{51}$$

In region II, this pressure field is

$$P^{II} = \rho_f \omega^2 \sum_\alpha c_\alpha^+ \phi_f(k_\alpha, r) e^{ik_\alpha z} \ , \quad z > L \ . \tag{52}$$

In Eqs. (51) and (52), the sum is over all the modes found from Eq. (8), and the axial distance z is measured from the upper fracture surface. In calculating the synthetics, Eqs. (51) and (52) are convolved with a wave source. We use a Kelly source (Kelly et al., 1976; Stephen et al., 1985) in this study. Given a center frequency ω_0 of the source, the maximum frequency ω_{max} is chosen as 2.5 ω_0. Starting from ω_{max}, we calculate the amplitude coefficients b_α^- and c_α^+ of each wave mode for each decreasing frequency. After Eqs. (51) and (52) are evaluated for each frequency, we multiply them with the source spectrum and inverse Fourier transform the products into time domain to generate waveforms for each given distance z in regions I and II. In this way, synthetic microseismograms are obtained which display the wave characteristics in the vicinity of a fracture.

RESULTS AND DISCUSSION

In this section, we present the theoretical results on the effects of a horizontal fracture on the propagation of borehole guided waves. The results will be given for the Stoneley

and pseudo-Rayleigh waves, respectively. In our calculations, the borehole radius is $a = 10$ cm and the rigid boundary is set at $d = 130$ cm. The formation properties are $V_p = 5$ km/s, $V_s = 3$ km/s, and $\rho = 2.5$ g/cm^3. For the fluid, we use $V_f = 1.5$ km/s and $\rho_f = 1$ g/cm^3. In the summation of the modes, we truncate the mode series by neglecting those modes whose k_α values are on the imaginary k axis, since they are not traveling waves (see Nolet et al., 1989 and Tsang, 1985, 1987).

Stoneley Wave

We first investigate the effects of the fracture on the incidence of Stoneley waves. Before presenting the results in more detail, it is instructive to compare the present theory with the previous models of Tang and Cheng (1989) and Hornby et al. (1989). Summarized briefly, these models consider the incidence of low frequency Stoneley waves on a fracture. The fracture is modeled as a fluid layer bounded by the rigid wall. Stoneley attenuation occurs because of the fluid flow into the rigid fracture. In Figure 2, we plot the transmission coefficients from the two models in a low frequency range of [0,5] kHz for a set of fracture apertures ranging from 0.5 cm to 5 cm. The two models are qualitatively similar in this low frequency range. Both models predict that the transmission across the fracture is reduced as the fracture aperture increases. The major significant difference is at low frequencies. Although both models show the decrease of transmission with decreasing frequency for each given aperture, the present theory predicts a greater decrease than the previous theory does. This discrepancy is due to the assumption of the rigid fracture wall in the previous theory. The present theory takes into account the elasticity of the wall by using Eq. (43), in which the wavenumber k_{f_T} is found by solving a period equation corresponding to the elastic fracture (Tang et al., 1989). The effects of mode conversion have also been checked. We found that the number of modes found from Eq. (8) decreases with decreasing frequency, as pointed out by Tsang (1985, 1987), and that the amplitudes of the radiation modes are considerably smaller compared with that of the Stoneley mode at low frequencies. This means that the energy converted to radiation is small. We therefore conclude that, at low frequencies, the transmission of Stoneley waves across a fracture is mainly controlled by the amount of fluid flow into the fracture.

Next we present the theoretical results in a higher frequency range of [0,15] kHz. Figure 3 shows the transmission (a) and reflection (b) coefficients of Stoneley waves in this frequency range for a set of fracture thicknesses, the thicknesses being indicated on each curve of this figure. At low frequencies, the characteristic decrease in transmission and increase in reflection indicate the fluid flow effects, as discussed previously. At higher frequencies (above 5 kHz), the transmission decreases and reflection increases. These effects are closely related to the increasing coupling of the Stoneley mode with radiation modes, since the number and amplitude of the latter modes increase as frequency increases. These effects are not predicted by the previous theory

since mode coupling was not considered. As frequency crosses the cut-off frequency of the first pseudo-Rayleigh mode, the transmission and reflection coefficients exhibit a discontinuous feature across the cut-off. The discontinuity is small for small fracture thickness (one can see this from the 0.5 cm and 1 cm curves), but becomes prominent as thickness increases. This discontinuity indicates the strong coupling of the Stoneley mode with the pseudo-Rayleigh mode. Because both modes are guided waves trapped in the borehole, the conversion of Stoneley wave energy to pseudo-Rayleigh energy is more efficient than the conversion to radiation modes, for the latter conversion occurs mostly at the fracture surfaces where the Stoneley energy is not as significant as in the borehole. To illustrate Stoneley wave characteristics due to a fracture as a function of frequency, we calculate synthetic microseismograms with different source center frequencies and show the results in Figures 4 and 5. In Figure 4 , the source center frequency is 12 kHz, while the cut-off frequency of the first pseudo-Rayleigh wave mode is 8.36 kHz for the model used. Thus the coupling of the Stoneley with this wave mode is expected. Figure 4a shows the synthetics for a 1 cm thick fracture whose location is indicated by an arrow on the fracture-receiver offset axis. A Stoneley wave is generated at $z = -1.2$ m from the fracture and then incident on it from the negative z direction. In both (a) and (b) of Figure 4, we expand the scale for the amplitude to show the small amplitude converted waves. As can be seen from Figure 4a, the Stoneley wave impinging on the fracture is largely transmitted and partly reflected, in accordance with the transmission and reflection coefficients shown on Figure 3. In addition, there is some small amplitude wave energy originating from the fracture. The early portions of these waves move out above and below the fracture at the formation shear velocity (indicated by the solid lines). Following them are the strongly dispersive pseudo-Rayleigh waves. This example shows that, in addition to the transmission and reflection effects, a small portion of the Stoneley waves is converted to pseudo-Rayleigh waves at the fracture. In the next example, we increase the fracture aperture to 4 cm and keep other parameters unchanged. The resulting synthetics are shown in Figure 4b. This figure exhibits much stronger converted pseudo-Rayleigh waves than those shown on Figure 4a, because of the increased Stoneley to pseudo-Rayleigh conversion due to the much thicker fracture. Using the synthetic examples, we have demonstrated that the discontinuity in transmission and reflection coefficients shown in Figure 3 is due to the coupling of Stoneley with pseudo-Rayleigh waves. We now study the Stoneley waves below the cut-off frequency. In Figure 5a, the fracture aperture is still 4 cm, as used in Figure 4b, but the source center frequency is reduced to 5 kHz. Around this frequency, the major wave is the Stoneley mode, together with a number of small amplitude radiation modes. The synthetics in Figure 5a show that, at low frequencies, the mode conversion effects are minimal and the major effects are the transmission and reflection of the Stoneley mode according to the the coefficients given in Figure 3a and Figure 3b. As an extremal example, we show the synthetics corresponding to very low frequency tube (Stoneley) waves. In Figure 5b, the source frequency is only 300 Hz, and the fracture aperture is 2 cm. A Stoneley wave is generated at $z = -13$

m from the fracture and incident on it from the negative z direction. We can notice the strong Stoneley reflection from the fracture and the significant attenuation of the transmitted waves across the fracture. These phenomena are commonly observed in VSP measurements where low frequency tube waves are often excited (Hardin et al., 1987). The important implication of this example to field measurements is that the strong, coherent low frequency tube wave reflections are often associated with a fracture. Thus they may be used to provide useful information for fracture detection and characterization.

Pseudo-Rayleigh Wave

pseudo-Rayleigh waves comprise an important portion of full waveform acoustic logs following the onset of formation of shear arrivals. Because these wave modes are more intimately coupled with the formation than the Stoneley (Stephen et al., 1985), they may be more sensitive to a formation fracture than the Stoneley wave.

Figure 6 shows the transmission (a) and reflection (b) coefficients of the first two pseudo-Rayleigh modes in the frequency range of [7,21] kHz for three different fracture apertures, which are 0.1 cm, 1 cm, and 2 cm, respectively. The apertures are chosen to model very thin ($L = 0.1$ cm) and relatively thick ($L = 2$ cm) borehole fractures. The parameters for the calculations are the same as those used for the Stoneley wave calculations. A prominent feature shown in Figure 6a is that, for all apertures, thin or thick, the pseudo-Rayleigh waves are strongly attenuated across the borehole fracture, the second mode being more attenuated than the first one. This behavior of pseudo-Rayleigh waves is very different from that of the Stoneley wave shown in Figure 3a. This difference can be expected from the wave motion characteristics of the two waves. The Stoneley wave is mostly borne in the borehole fluid and its particle motion is dominantly in the axial direction. As has been shown previously, apart from some energy loss due to mode coupling at higher frequencies, the attenuation of the Stoneley by a fracture is due largely to the fluid flow into the fracture driven by this wave motion. Whereas for the pseudo-Rayleigh wave, the particle motion at the borehole interface is of elliptical shape and is dominated by horizontal motion (Stephen et al., 1985). This kind of wave motion requires the formation shear strength to sustain its propagation. Consequently, when this wave motion encounters a crack filled with material of zero shear strength, this motion picture will be destroyed. Thus, as long as there is no shear coupling between the fracture surfaces, pseudo-Rayleigh waves will be significantly affected, whatever the fracture thickness. This is what we have seen in Figure 6a. Moreover, for the transmitted energy, it may take a while for this energy to organize its elliptically shaped wave motion and become reguided. Thus, after being transmitted across a fracture, the pseudo-Rayleigh wave may disappear for a while before it reappears as a guided wave, leaving a blank part on the acoustic logs. This characteristic will later be illustrated with laboratory examples. Another inter-

esting feature in Figure 6a is that as the frequency decreases to approach the cut-off frequency, the transmission coefficients also decrease, the first mode being more drastic. This decrease in transmission will make the severely attenuated pseudo-Rayleigh waves even weaker near the cut-off frequencies. This characteristic has been observed in the laboratory and will be shown in the next section. This characteristic may also have some implications in detecting borehole fractures using acoustic logs. Because the phase and group velocities of the pseudo-Rayleigh wave reach their maximum value at the cut-off frequency, which is the formation shear velocity V_s (Cheng et al., 1981), the early arrivals of this wave are the wave energy near the cut-off frequencies. Therefore, on an acoustic log, if one traces the formation shear arrival times across a fracture, the lack of wave energy following these arrival times may be a very good indicator of the existing fracture. We now take a look at the reflection coefficients shown on Figure 6b. The reflection of the pseudo-Rayleigh waves by a fracture is strong even for the very thin fracture with thickness of 0.1 cm. The reflection increases towards the cut-off, corresponding to the decrease of the transmission coefficient shown in Figure 6a. However, as the aperture varies from the very thin to relatively thick fractures, the reflection coefficient does not change significantly, especially for the first mode at higher frequencies. This is in agreement with the finite difference modeling of Stephen (1986). In his modeling, the source frequency is between the cut-off of the first pseudo-Rayleigh mode and that of the second mode. For different fracture apertures, he obtained reflected pseudo-Rayleigh waves with practically the same amplitude. Thus, thin fractures are practically as effective as thick fractures in decoupling the pseudo-Rayleigh waves from the lower formation. The reflected pseudo-Rayleigh waves, when not seriously contaminated by later arrivals of incident waves, may also be an indication of the existence of borehole fractures.

LABORATORY EXPERIMENTAL STUDIES

Laboratory experiments were performed to study the propagation characteristics of borehole guided waves across a horizontal fracture. These experiments also provide a test of the theoretical analysis of this study.

Experimental Procedure

Two aluminum cylinders were used, each having a height of 12 cm and diameter of 20 cm. The compressional and shear velocities of this material are $V_p = 6.4$ km/s and $V_s = 3.1$ km/s, respectively. Its density is 2.7 g/cm^3. A borehole of 1 cm diameter was drilled at the center of each cylinder. A horizontal fracture is simulated by a gap between the smooth ends of the two cylinders, as shown in Figure 1. By varying the thickness of the gap, we can measure the effects of the fracture aperture on the borehole

acoustic waves. In the experiment, an acoustic transducer is mounted at the bottom of the model and a receiver with a diameter of 0.9 cm is placed in the borehole to measure the waves. Because of its size, the receiver measures the average incoming wave field over the borehole area and, when the source and receiver are on the same side of the fracture, the receiver is not sensitive to the waves reflected back from the fracture. In other words, the experiment detects the effects of the fracture by measuring the transmission of borehole acoustic waves. During the experiment, the model assembly is submerged in a water tank. The water acoustic velocity is 1.5 km/s and its density 1 g/cm^3. The receiver is initially placed below the fracture. After a waveform is recorded, the receiver is moved to next position by a step motor controller at a step length of 0.18 mm. In this process, the receiver passes the fracture and eventually moves above it. The whole process generates a waveform array. This array is processed by stacking the desired signal at its move-out velocity. If the desired signal is not the dominant wave in the data (for example, the pseudo-Rayleigh wave may be followed by strong Stoneley arrivals), windowing the signal may become necessary. The stacked signals below and above the fracture give the average incident and transmitted waves. The amplitude spectral ratio of the incident wave relative to that of the transmitted wave in the frequency range of interest gives the transmission coefficient across the fracture in that frequency range.

Experimental Results

We first show the experimental results for the Stoneley waves. Figure 7 shows the experimental array waveform data of Stoneley waves. The waves were recorded below the cut-off frequency of the first pseudo-Rayleigh wave (which is about 174 kHz for the model used), so that the Stoneley waves are the strongest phase in the data. For this example, the fracture has an aperture of 2.8 mm. Its location is indicated in Figure 7 on the source-receiver offset axis . It can be seen that the transmitted wave amplitude is reduced by the fracture. Figure 8a shows the averaged incident and transmitted wave spectra obtained by respectively stacking the wave traces above and below the fracture. The reduction of the transmitted wave amplitude is clearly seen in the frequency range of about 90–180 kHz, in which the wave amplitude is the strongest. Figure 8b shows the ratio of the transmitted amplitude relative to the incident amplitude in the same frequency range. The theoretical transmission coefficient is also plotted. The measured data and the theory are in good agreement. As another example, Figure 8 also shows the incident and transmitted wave spectra (c) and the measured transmission coefficient versus the theoretical coefficient (d) obtained for a 5.1 mm thick laboratory model fracture. Again, in the same frequency range, the measured transmission coefficient and the theoretical transmission coefficient are in good agreement. We performed the experiments for a set of model fractures with thickness ranging from 0.2 to 5.1 mm. We then averaged the theoretical and experimental transmission coefficients in the

frequency range around 135 kHz, as shown in (b) and (d) of Figure 8. The averaged results are plotted versus fracture thickness in Figure 9 . They agree very well. As can be seen from this figure, the transmission coefficient decreases with increasing fracture aperture. This result agrees with those of the previous experiments given in Tang and Cheng (1989) and Hornby et al. (1989).

In our experiment, we extend the measurements to pseudo-Rayleigh waves to study their response to the effects of a fracture and to test the theoretical predictions. In order to effectively excite pseudo-Rayleigh waves, we performed the experiments in a higher frequency range around 330 kHz. Figure 10 shows the array waveforms for the laboratory measurements with fracture aperture equal to 0.3 mm (a) and 2.5 mm (b), respectively. In (a) and (b) of this figure, we expand the scale for the wave amplitude to highlight the pseudo-Rayleigh waves (denoted by P-R in this figure), particularly the transmitted waves. A line across the array (denoted by S) indicates the formation shear arrival time of each trace. The location of the fracture is also indicated by an arrow on offset axis. In fact, the array waveforms for the two very different fracture apertures are very similar. For the upper part of the array (incident waveforms), the pseudo-Rayleigh waves are effectively excited. Following them are some high-frequency fluid arrivals which are mixed up with the pseudo-Rayleigh waves. However, right after being transmitted across the fracture, the pseudo-Rayleigh portion of the waveforms is drastically attenuated, leaving a region with very emergent wave energy. At some distance farther from the fracture, the waves become reguided and reappear as coherent pseudo-Rayleigh waves. One may also notice that the early part of these waves following the formation shear arrival times (indicated by the line across the array) is very weak compared with the early part of the incident waves. The fact that the above described phenomena are common for both the thin (L=0.3 mm) and the thick (L=2.5 mm) fractures agrees with the theoretical prediction that a thin fracture is as effective as a thick fracture in affecting pseudo-Rayleigh waves. As discussed previously, after the elliptically-shaped particle motion is destroyed at the fracture, the propagating pseudo-Rayleigh energy may take a while to organize its original motion and become reguided. This is demonstrated by the almost blank region across the fracture in both (a) and (b) of Figure 10. The weak early arrivals of the transmitted waves are the wave energy near the cut-off frequencies. Their small amplitude compared with that of the incident waves also agrees with the theoretical result that the transmission coefficient is generally the smallest near the cut-off frequencies. To make a quantitative comparison between the experiment and the theory, we need to process the data of Figure 10. We first window the pseudo-Rayleigh waves before the fluid arrivals. Then we stack the upper part of the windowed array to obtain the average incident waveform. For the lower part that corresponds to the transmitted waves, we stack the last 9 traces which consist of coherent pseudo-Rayleigh energy. This gives the average transmitted waveform. The results of the processing are shown in Figure 11 for the L=0.3 mm (a) and L=2.5 mm (b) fractures. In this figure, the formation shear arrival times are marked on each waveform, and the transmitted wave amplitude is scaled relative

to the maximum incident amplitude. As can be seen from this figure, the relative amplitudes of the transmitted and the incident waves in both (a) and (b) are very similar, despite the fact the one fracture (L=2.5 mm) is more than 8 times as thick as the other (L=0.3 mm). Moreover, for the transmitted waves in both (a) and (b), there is some weak energy following the formation shear arrival times, indicating the strong attenuation of pseudo-Rayleigh waves near the cut-off frequencies. Figure 12 shows the amplitude spectra (a and c) of the waves shown in Figures 10a and b and the resulting transmission coefficients (open circles on (b) and (d) of Figure 12) obtained from the spectral ratio of the transmitted spectrum relative to the incident spectrum. The theoretical transmission coefficients (solid line) are also plotted. Because the first three cut-off frequencies for the laboratory borehole model are at 174.2, 258.1, and 403.3 kHz, respectively, the measured experimental pseudo-Rayleigh waves around 330 kHz are dominated by the contribution from the second mode. Therefore, the theoretical results are calculated for this wave mode. As shown on Figures 12b and d, theory and experiment agree in both cases. Both results show the same amount of amplitude attenuation of the transmitted waves and the general decreasing tendency of the transmission coefficient towards the cut-off frequency. The experiments on the pseudo-Rayleigh waves have shown the wave characteristics across an open horizontal fracture and confirmed theoretical analysis on these waves.

CONCLUSIONS

In this study, we have investigated the propagation of borehole guided waves across an open horizontal fracture. The theoretical analysis was based on a hybrid method (Tsang, 1985, 1987). This method generates wave modes which are summed to match the boundary conditions at the fracture surfaces. To overcome the singularity problem in matching the surface conditions, we balance the borehole fluid flow across and into the fracture, as we have done for the Stoneley waves (Tang and Cheng, 1989). The coupling at the fracture surfaces results in the transmission and reflection of an incident borehole guided wave. Based on our analysis, we have calculated the transmission and reflection coefficients due to a fracture for the Stoneley and pseudo-Rayleigh waves. It has been shown that, at low frequencies, the effects of the fracture on the Stoneley wave are controlled by the amount of fluid flow into the fracture. This has been confirmed by the laboratory measurements on Stoneley waves. As frequency increases, the effects of mode conversion at the fracture become important. Particularly above the the cut-off frequency of the first pseudo-Rayleigh mode, the conversion to pseudo-Rayleigh wave is significant, especially for a thick fracture, as has been shown by synthetic microseismograms. For the pseudo-Rayleigh wave, an open fracture, whatever the thickness, drastically reduces the transmitted wave amplitude and produces strong reflection, these effects being more significant towards the cut-off frequencies than away from these frequencies. As shown by the laboratory measurements

performed using thin and thick fractures, because of the destruction of its elliptically-shaped particle motion at the fracture, the transmitted pseudo-Rayleigh wave leaves a region with very weak wave energy in the vicinity of the fracture. This characteristic may be an important indication of the existence of an open fracture on an acoustic log. In addition, laboratory experiments also indicated the weak early arrivals of the transmitted pseudo-Rayleigh waves, as predicted by the theory. In general, the theory and experiment agree quite well. The guided wave characteristics due to a fracture described in this study may provide useful information for the fracture detection and characterization using acoustic logs.

ACKNOWLEDGEMENTS

This research was supported by the Full Waveform Acoustic Logging Consortium at M.I.T. and by Department of Energy grant No. DE-FG02-86ER13636.

REFERENCES

Brie, A., K., Hsu, and C. Eckersley, 1988, Using the Stoneley normalized differential energies for fractured reservoir evaluation; *Trans. 29th SPWLA Ann. Logging Symp.*, San Antonio, TX, XX1-XX25.

Bhashvanija, K., 1983, A finite difference model of an acoustic logging tool: The borehole in a horizontal layered geologic medium, Ph.D. Thesis, Colorado School of Mines, Golden, CO.

Cheng, C.H., and M.N. Toksöz, 1981, Elastic wave propagation in a fluid-filled borehole and synthetic acoustic logs; *Geophysics, 46*, 1042-1053.

Delves, L.M., and J. Walsh, 1974, *Numerical Solution of Integral Equations*, Oxford: University Press.

Haddon, R.A., 1987, Numerical evaluation of Green's function for axisymmetric boreholes using leaking modes: *Geophysics, 52*, 1099-1105.

Haddon, R.A., 1989, Exact Green's functions using leaking modes for solid elastic media; *Geophysics, 54*, 609-620.

Hardin, E.L., C.H. Cheng, F.L. Paillet, and J.D. Mendelson, 1987, Fracture characterization by means of attenuation and generation of tube waves in fractured crystalline rock at Mirror Lake, New Hampshire; *J. Geophys. Res., 92*, 7989-8006.

Hsu, K., A. Brie, and R.A. Plumb, 1985, A new method for fracture identification using array sonic tools; *Rep. 14397*, Soc. of Petrol. Engineer.

Hornby, B.E., D.L. Johnston, K.H. Winkler, and R.A. Plumb, 1989, Fracture evaluation using reflected Stoneley-wave arrivals; *Geophysics, 54*, 1274-1288.

Kelly, K.R., R.W. Ward, S. Treitel, and R.M. Alford, 1976, Synthetic microseismograms: A finite-difference approach; *Geophysics, 41*, 2-27.

Morse, P.M., and H. Feshbach, 1953, *Methods of Theoretical Physics*, New York, McGraw-Hill Book Company.

Nolet, G., R. Sleeman, V. Nijhof, and B.L.N. Kennett, 1989, Synthetic reflection microseismograms in three dimensions by a locked-mode approximation; *Geophysics, 54*, 350-358.

Paillet, F.L., 1980, Acoustic propagation in the vicinity of fractures which intersect a fluid-filled borehole, *Trans. SPWLA 21th Annu. Symp.*, Paper DD, 33p.

Stephen, R.A., F. Pardo-Casas, and C.H. Cheng, 1985, Finite difference synthetic

acoustic logs; *Geophysics, 50*, 1588-1609.

Stephen, R.A., 1986, Synthetic acoustic logs over bed boundaries and horizontal fissures; M.I.T. Full Waveform Acoustic Logging Consortium Annual Report.

Tang, X.M., and C.H. Cheng, 1989, A dynamic model for fluid flow in open borehole fractures; *J. Geophy. Res., 94*, 7567-7576.

Tang, X.M., C.H. Cheng, and M.N. Toköz, 1989, Stoneley wave propagation in a fluid-filled borehole with a vertical fracture; M.I.T. Full Waveform Acoustic Logging Consortium Annual Report.

Tsang, L., 1985, Solution of the fundamental problem of transient acoustic propagation in a borehole with the hybrid method; *J. Acoust. Soc. Am., 77*, 2024-2032.

Tsang, L., 1987, Transient acoustic waves in a fluid-filled borehole with a horizontal bed boundary separating two solid formations; *J. Acoust. Soc. Am., 81*, 844-853.

APPENDIX A

In this Appendix, we list the displacement and stress components for the formation and borehole fluid. These components are:
For the fluid:

$$u_{zf} = ikAI_0(fr) \ , \tag{A-1}$$
$$u_{rf} = fAI_1(fr) \ , \tag{A-2}$$
$$\sigma_{zzf} = -\rho_f^2\omega^2 AI_0(fr) \ . \tag{A-3}$$

For the formation:

$$u_{rs} = l[-BK_1(lr) + B'I_1(lr)] - ik[CK_1(mr) + C'I_1(mr)] \ , \tag{A-4}$$
$$u_{zs} = ik[BK_0(lr) + B'I_0(lr)] + m[-CK_0(mr) + C'I_0(mr)] \ , \tag{A-5}$$
$$\sigma_{zzs} = -(\rho\omega^2 + 2\mu l^2)[BK_0(lr) + B'I_0(lr)] + 2\mu ikm[-CK_0(mr) + C'K_0(mr)] \ , \tag{A-6}$$
$$\sigma_{rzs} = 2\mu ikl[-BK_1(lr) + B'I_1(lr)] + (k^2 + m^2)\mu[CK_1(mr) + C'I_1(mr)] \ , \tag{A-7}$$
$$\sigma_{rrs} = B[(-\rho\omega^2 + 2\mu k^2)K_0(lr) + 2\mu(l/r)K_1(lr)] + B'[(-\rho\omega^2 + 2\mu k^2)I_0(lr) - 2\mu(l/r)I_1(lr)]$$
$$+2\mu ikmC[K_0(mr) + K_1(mr)/(mr)] - 2\mu ikmC'[I_0(mr) - I_1(mr)/(mr)] \ . \tag{A-8}$$

Note that every equation in this Appendix has the $exp(ikz)$ dependences.

APPENDIX B

In this Appendix, we give the matrix elements of Eq. (7) as follows.

$$a_{11} = k_f^2 I_0(fa) \ , \tag{B-1}$$
$$a_{12} = [(\lambda/\lambda_f)(l^2 - k^2) + 2(\mu/\lambda_f)l^2]K_0(la) + 2(\mu/\lambda_f)(l/a)K_1(la) \ , \tag{B-2}$$
$$a_{13} = 2(\mu/\lambda_f)ikm[K_0(ma) + K_1(ma)/(ma)] \ , \tag{B-3}$$
$$a_{14} = [(\lambda/\lambda_f)(l^2 - k^2) + 2(\mu/\lambda_f)l^2]I_0(la) - 2(\mu/\lambda_f)(l/a)I_1(la) \ , \tag{B-4}$$
$$a_{15} = -2(\mu/\lambda_f)ikm[I_0(ma) - I_1(ma)/(ma)] \ , \tag{B-5}$$
$$a_{21} = fI_1(fa) \ , \tag{B-6}$$
$$a_{22} = lK_1(la) \ , \tag{B-7}$$
$$a_{23} = ikK_1(ma) \ , \tag{B-8}$$
$$a_{24} = -lI_1(la) \ , \tag{B-9}$$
$$a_{25} = ikI_1(ma) \ , \tag{B-10}$$
$$a_{32} = -2iklK_1(la) \ , \tag{B-11}$$
$$a_{33} = (k^2 + m^2)K_1(ma) \ , \tag{B-12}$$
$$a_{34} = 2iklI_1(la) \ , \tag{B-13}$$

$$a_{35} = (k^2+m^2)I_1(ma) \ , \tag{B-14}$$
$$a_{42} = ikK_0(ld) \ , \tag{B-15}$$
$$a_{43} = -mK_0(md) \ , \tag{B-16}$$
$$a_{44} = ikI_0(ld) \ , \tag{B-17}$$
$$a_{45} = mI_0(md) \ , \tag{B-18}$$
$$a_{52} = -lK_1(ld) \ , \tag{B-19}$$
$$a_{53} = -ikK_1(md) \ , \tag{B-20}$$
$$a_{54} = lI_1(ld) \ , \tag{B-21}$$
$$a_{55} = -ikI_1(md) \ . \tag{B-22}$$

APPENDIX C

In this Appendix, we give the analytical expressions for the integrals given in Eqs. (38) and (39). For the first integral, we make use of the expressions of σ_{zzf} and σ_{zzs} listed in Appendix A. Multiply them by $J_0(\zeta r)r$ (here we omit the subscripts α and n) and integrate over from 0 to a and a to d. This gives

$$\begin{aligned} I(k,\zeta) = \ & \zeta a J_1(\zeta a)[a_0/(\zeta^2+f^2)+a_1/(\zeta^2+l^2)+a_2/(\zeta^2+m^2)] \\ & +J_0(\zeta a)[b_0/(\zeta^2+f^2)+b_1/(\zeta^2+l^2)+b_2/(\zeta^2+m^2)] \\ & +J_0(\zeta d)[c_1/(\zeta^2+l^2)+c_2/(\zeta^2+m^2)] \ , \end{aligned} \tag{C-1}$$

where

$$a_0 = -\rho_f\omega^2 I_0(fa) \ , \tag{C-2}$$
$$a_1 = (\rho\omega^2+2\mu l^2)[BK_0(la)+B'I_0(la)] \ , \tag{C-3}$$
$$a_2 = 2\mu ikm[CK_0(ma)-C'I_0(ma)] \ , \tag{C-4}$$
$$b_0 = -\rho_f\omega^2 faI_1(fa) \ , \tag{C-5}$$
$$b_1 = (\rho\omega^2+2\mu l^2)la[-BK_1(la)+B'I_1(la)] \ , \tag{C-6}$$
$$b_2 = -2\mu ikm^2a[CK_1(ma)+C'I_1(ma)] \ , \tag{C-7}$$
$$c_1 = (\rho\omega^2+2\mu l^2)ld[BK_1(ld)-B'I_1(ld)] \ , \tag{C-8}$$
$$c_2 = 2\mu ikm^2d[CK_1(md)+C'I_1(md)] \ . \tag{C-9}$$

For the second integral, we use the σ^1_{zz} defined in Eq. (34). Applying the identity

$$J_0(\zeta r) = \frac{d}{dr}[rJ_1(\zeta r)]/(\zeta r) \tag{C-10}$$

to Eq. (39) and integrating by part, we get

$$I_1(k,\zeta) = \zeta^{-1}[rJ_1(\zeta r)\sigma^1_{zz}(k,r)]\Big|_0^d - \zeta^{-1}\int_0^d \frac{d}{dr}[\sigma^1_{zz}(k,r)]J_1(\zeta)rdr \ . \tag{C-11}$$

Because σ_{zz}^1 is continuous at $r = a$ and $J_1(\zeta d) = 0$ (Eq. 20), the first term vanishes. From Eq. (34), we can see that the derivative of σ_{zz}^1 equals that of σ_{zz}. Using σ_{zz} given in Appendix A and completing the integration of the second term, we obtain

$$\begin{aligned} I_1(k,\zeta) &= J_1(\zeta a)/\zeta[a_0'/(\zeta^2+f^2) + a_1'/(\zeta^2+l^2) + a_2'/(\zeta^2+m^2)] \\ &\quad + aJ_0(\zeta a)[b_0'/(\zeta^2+f^2) + b_1'/(\zeta^2+l^2) + b_2'/(\zeta^2+m^2)] \\ &\quad + dJ_0(\zeta d)[c_1'/(\zeta^2+l^2) + c_2'/(\zeta^2+m^2)] \ , \end{aligned} \tag{C-12}$$

where

$$a_0' = \rho_f\omega^2 f^2 a I_0(fa) \ , \tag{C-13}$$

$$a_1' = -(\rho\omega^2 + 2\mu l^2) l^2 a[BK_0(la) + B'I_0(la)] \ , \tag{C-14}$$

$$a_2' = 2\mu ikm^3 a[-CK_0(ma) + C'I_0(ma)] \ , \tag{C-15}$$

$$b_0' = -\rho_f\omega^2 f I_1(fa) \ , \tag{C-16}$$

$$b_1' = -(\rho\omega^2 + 2\mu l^2) l[BK_1(la) - B'I_1(la)] \ , \tag{C-17}$$

$$b_2' = -2\mu ikm^2[CK_1(ma) + C'I_1(ma)] \ , \tag{C-18}$$

$$c_1' = (\rho\omega^2 + 2\mu l^2) l[BK_1(ld) - B'I_1(ld)] \ , \tag{C-19}$$

$$c_2' = 2\mu ikm^2[CK_1(md) + C'I_1(md)] \ . \tag{C-20}$$

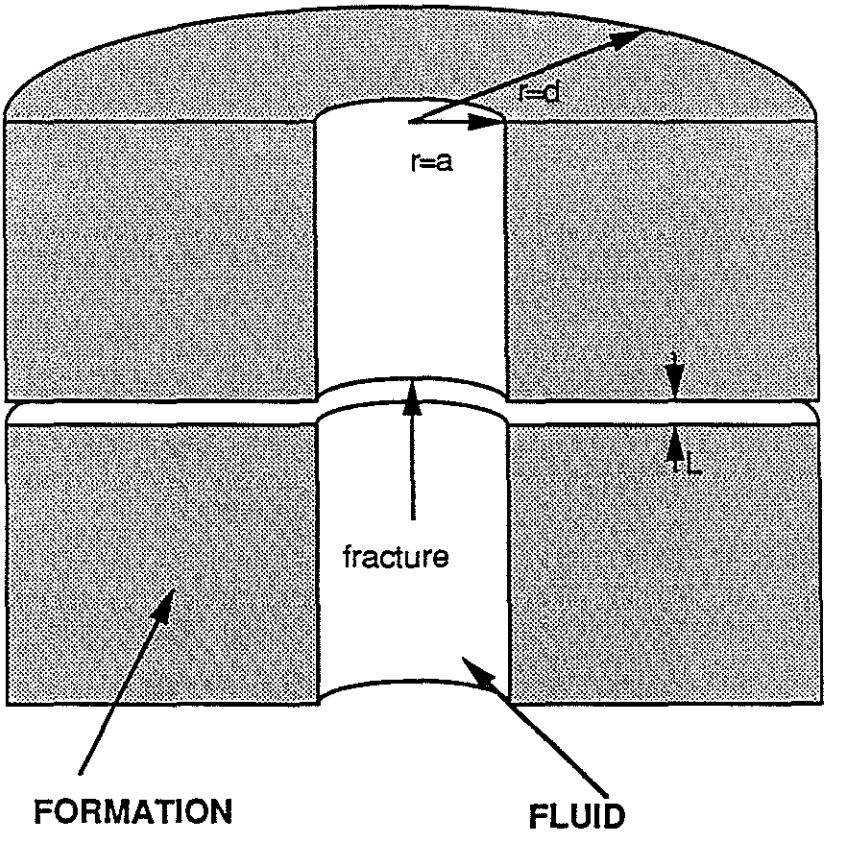

Figure 1: Borehole intersected by a horizontal fracture with thickness L. For the hybrid method, a rigid boundary is placed at $r = d \gg a$. The formation at both sides of the fracture is an elastic solid. The borehole and the fracture are filled with the same fluid.

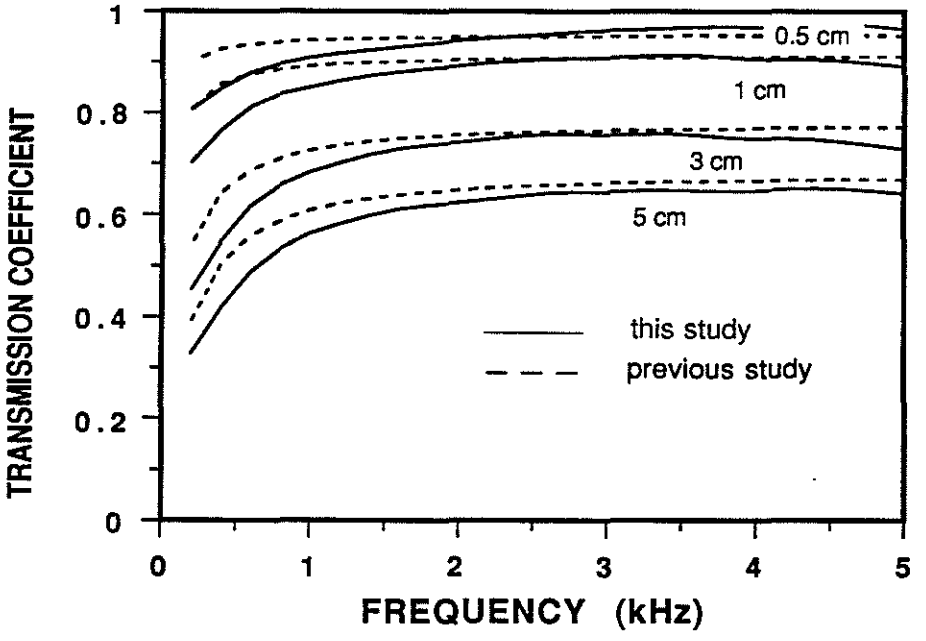

Figure 2: Comparison of the present theory (solid line) with the previous one (dashed line) for the transmission of Stoneley waves in the low frequency range. The model parameters are given in the text and the fracture apertures are indicated on the curves. At low frequencies, the present theory shows more attenuation than the previous theory.

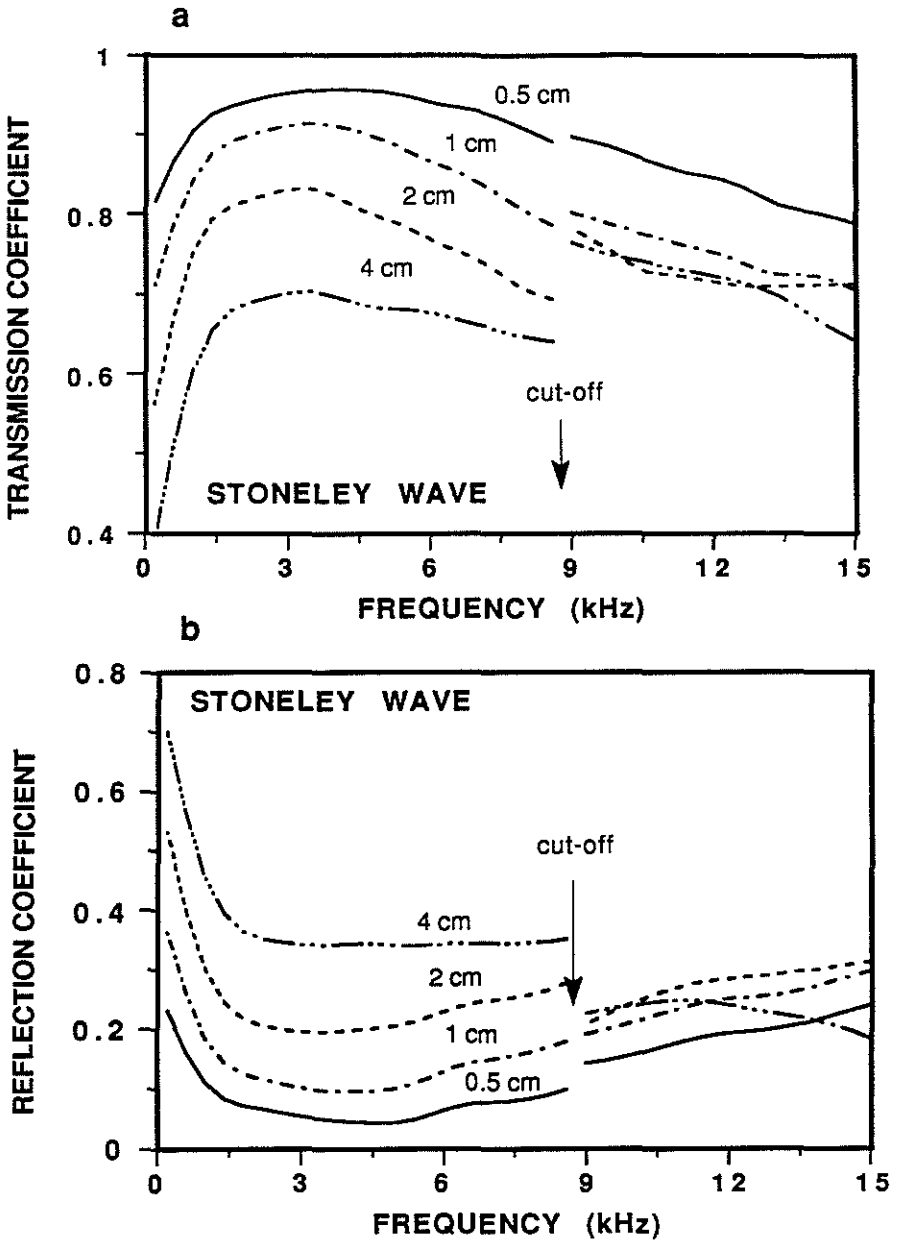

Figure 3: Transmission (a) and reflection (b) of Stoneley waves in the frequency range of [0,15] kHz. Above 5 kHz, the transmission decreases and reflection increases with frequency because of the coupling with radiation modes. At the cut-off frequency (marked by an arrow) the coefficients are discontinuous, indicating the coupling of the Stoneley with pseudo-Rayleigh waves.

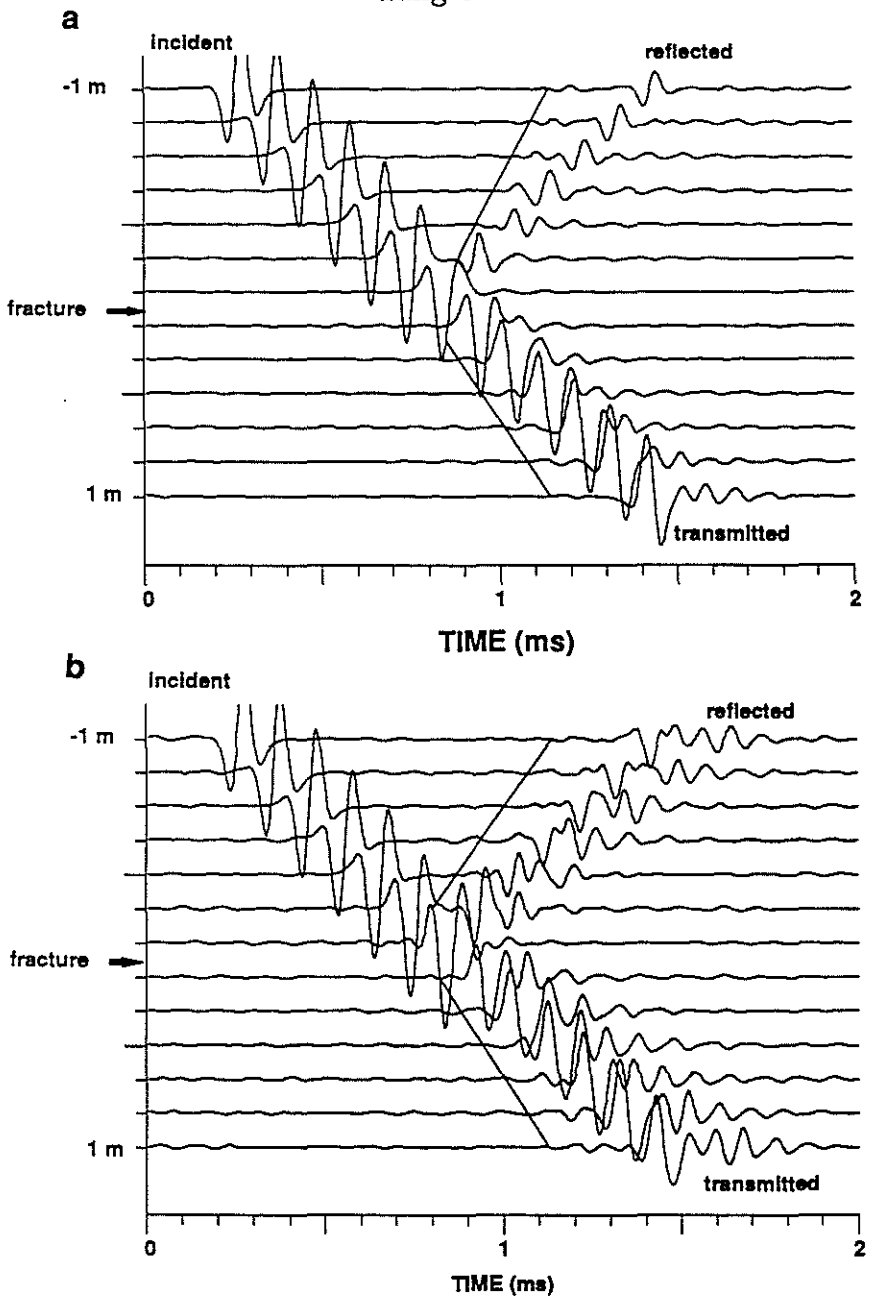

Figure 4: Synthetic microseismograms showing the conversion of Stoneley waves to pseudo-Rayleigh waves above the cut-off frequency. The Stoneley is the incident wave. In (a), the fracture aperture is 1 cm. In (b), it is 4 cm. The solid lines indicate the move-out of the formation shear signals originating from the fracture. Following them are the converted pseudo-Rayleigh waves. For the thicker fracture (b), the converted waves become stronger.

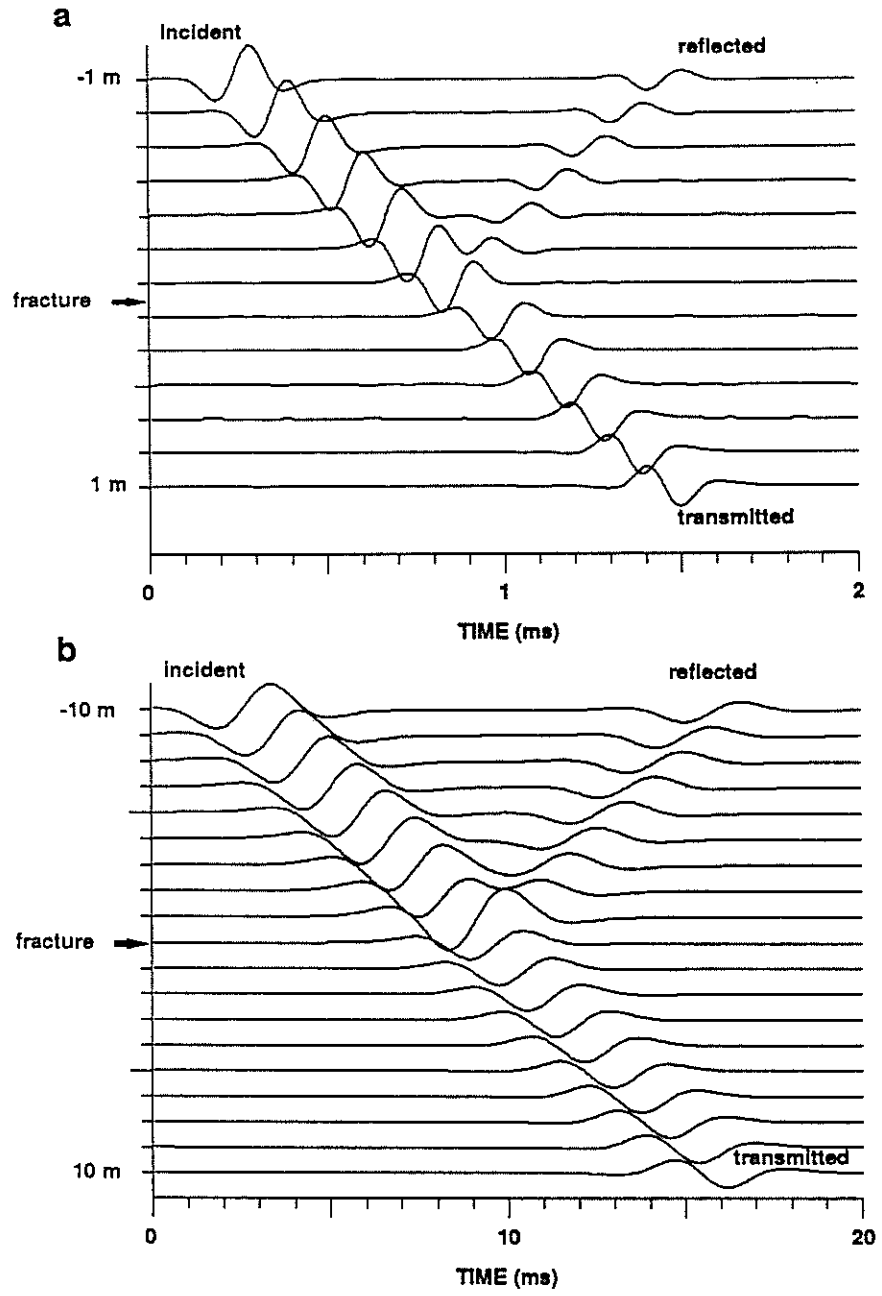

Figure 5: Stoneley waves below the cut-off frequency. In (a), the fracture aperture is 4 cm and source center frequency is 5 kHz. The Stoneley is simply transmitted and reflected at the fracture with little mode conversion effects. In (b), the fracture is 2 cm thick and the center frequency is down to 300 Hz to model tube waves observed in VSP measurements. The strong reflection and attenuation of the tube wave due to a fracture are common in such measurements.

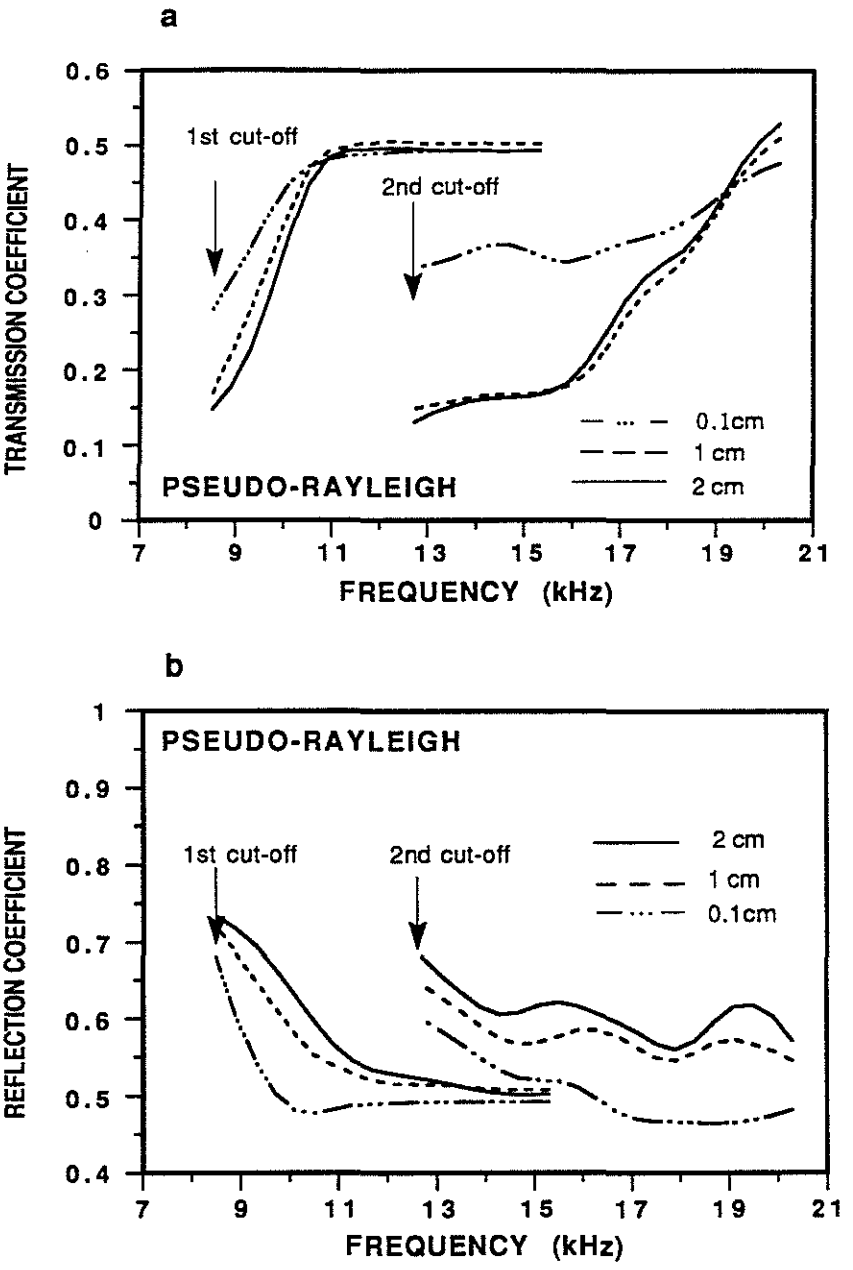

Figure 6: Transmission (a) and reflection (b) of the first two pseudo-Rayleigh modes as a function of frequency and fracture thickness. These types of wave modes are strongly attenuated and reflected by thin as well as thick fractures. Near the cut-off frequencies, the attenuation is generally the strongest.

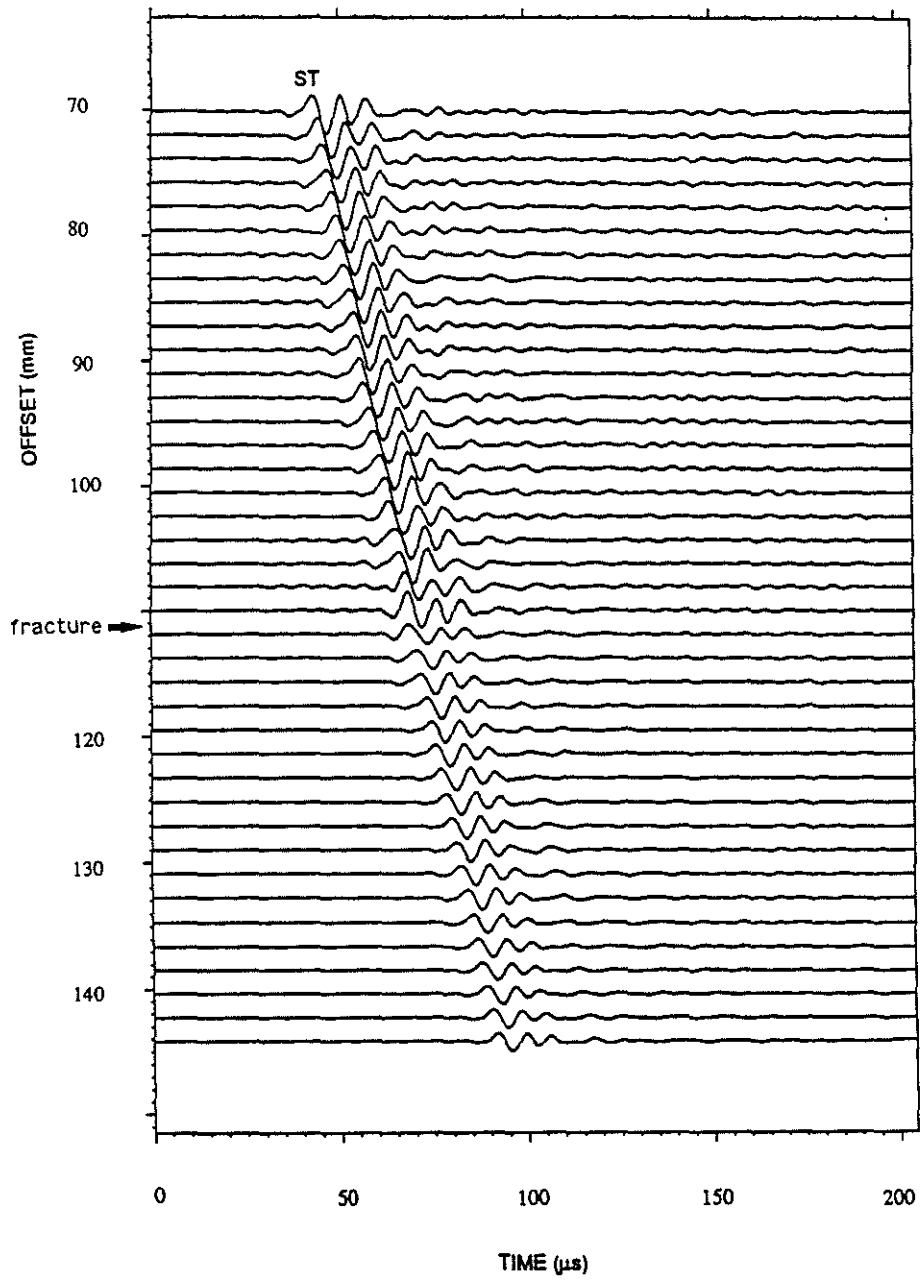

Figure 7: Experimental array waveform data for Stoneley waves. A fracture of 2.8 mm thick in the model is indicated on the offset axis. The Stoneley amplitude is reduced across the fracture.

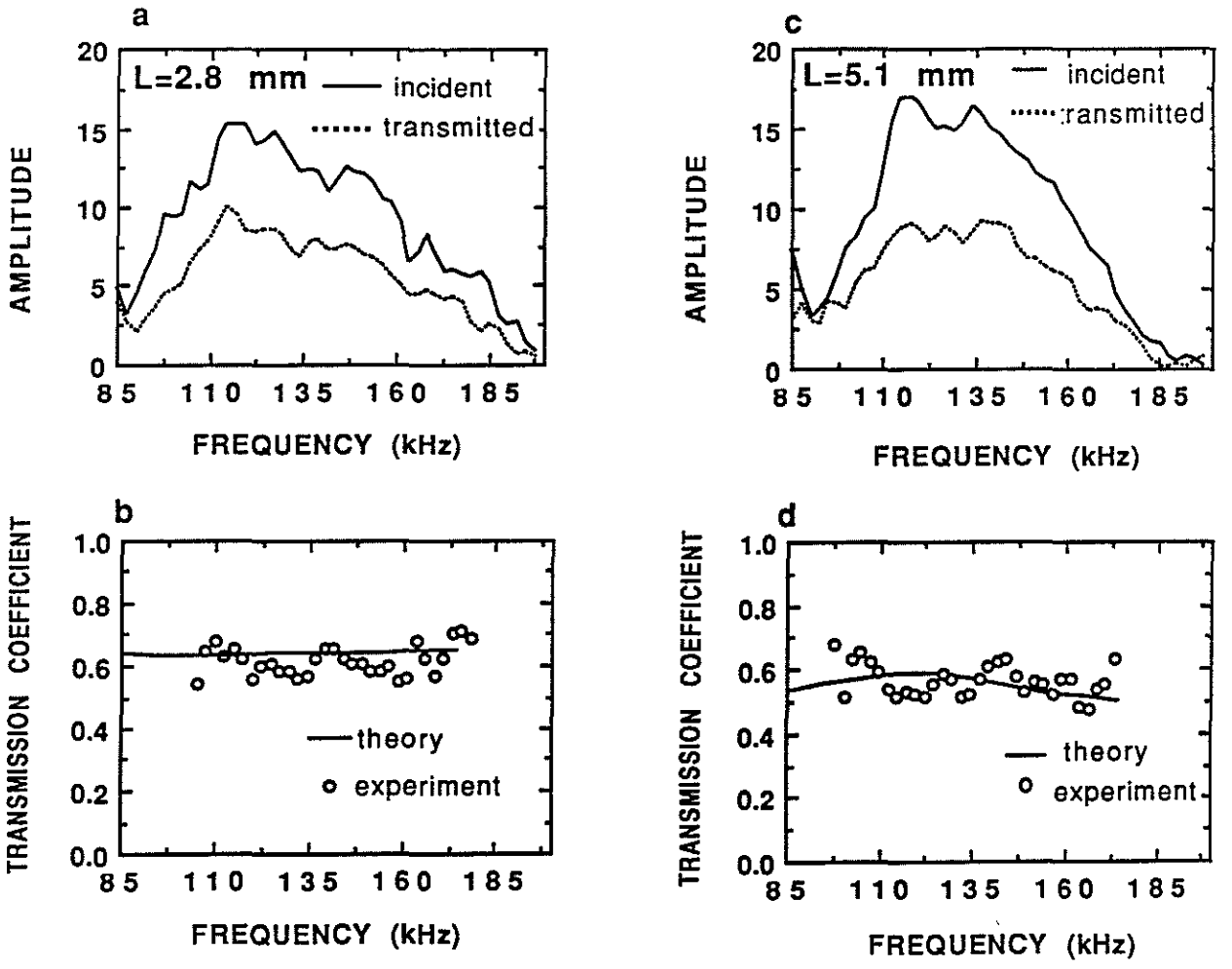

Figure 8: Experimental results from measurements with a 2.8 mm thick fracture (a and b) and a 5.1 mm thick one (c and d). The amplitude spectra of (a) and (c) show the reduction of wave amplitude across the fractures. The open circles in (b) and (d) are the measured transmission coefficient while the solid lines are the theoretical coefficient. The experiment and theory agree quite well.

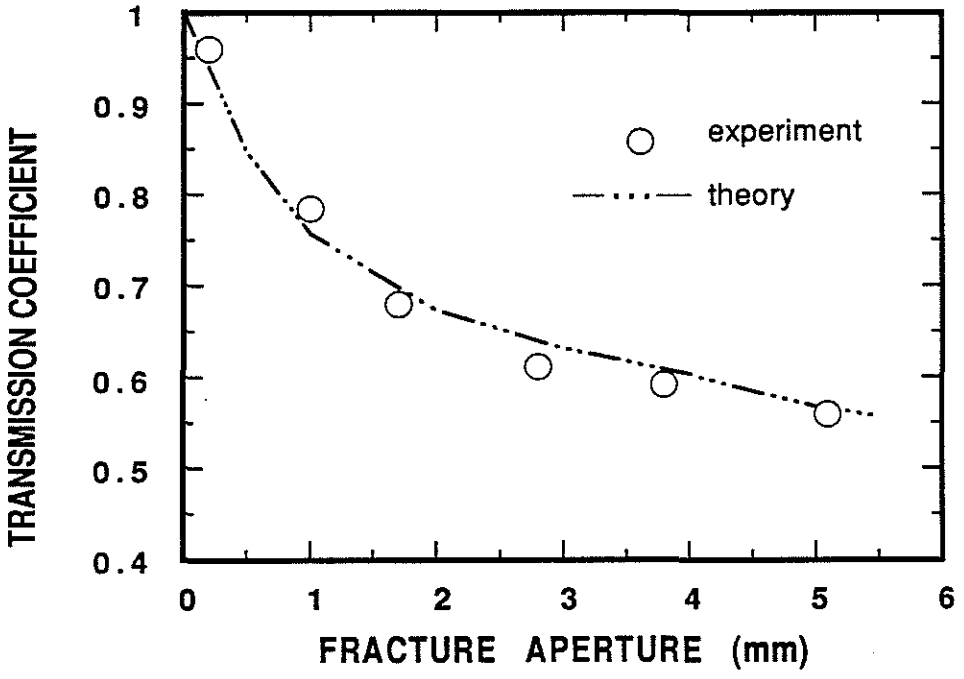

Figure 9: Experimental and theoretical transmission coefficients versus fracture thickness. These coefficients are averaged over the frequency range shown in Figure 8. The theory is in agreement with the experiment.

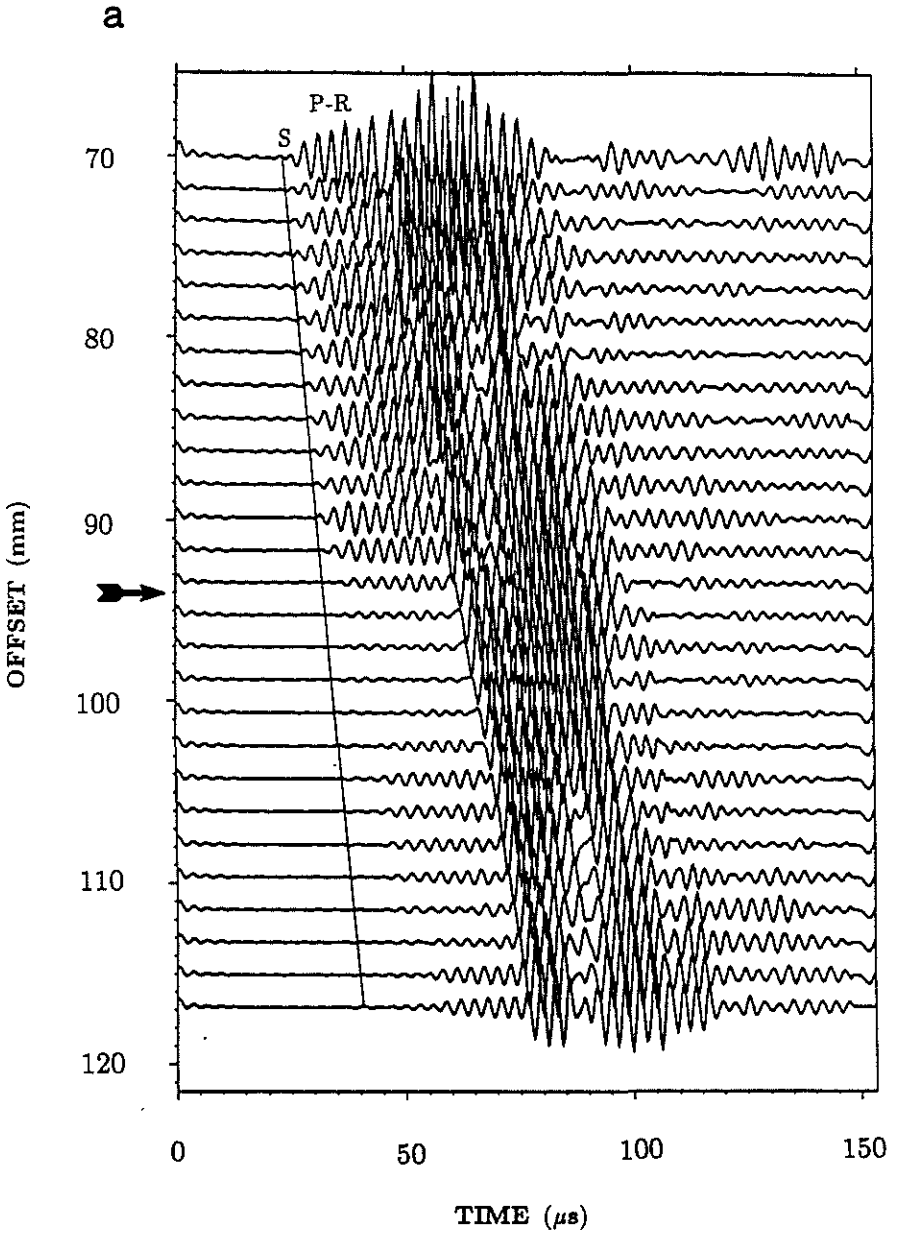

Figure 10: Experimental array waveform data for pseudo-Rayleigh waves. In (a), the fracture is 0.3 mm thick. In (b), it is 2.5 mm. The location of the fracture is indicated by an arrow. The pseudo-Rayleigh waves are denoted by P-R. A line across the array denoted by S indicates formation shear arrival times. The two sets of data are very similar although one fracture is much thicker than the other. Note the waves are missing across the fracture and become reguided at some distance away from it. Note also the lack of wave energy in the early part of the transmitted waves.

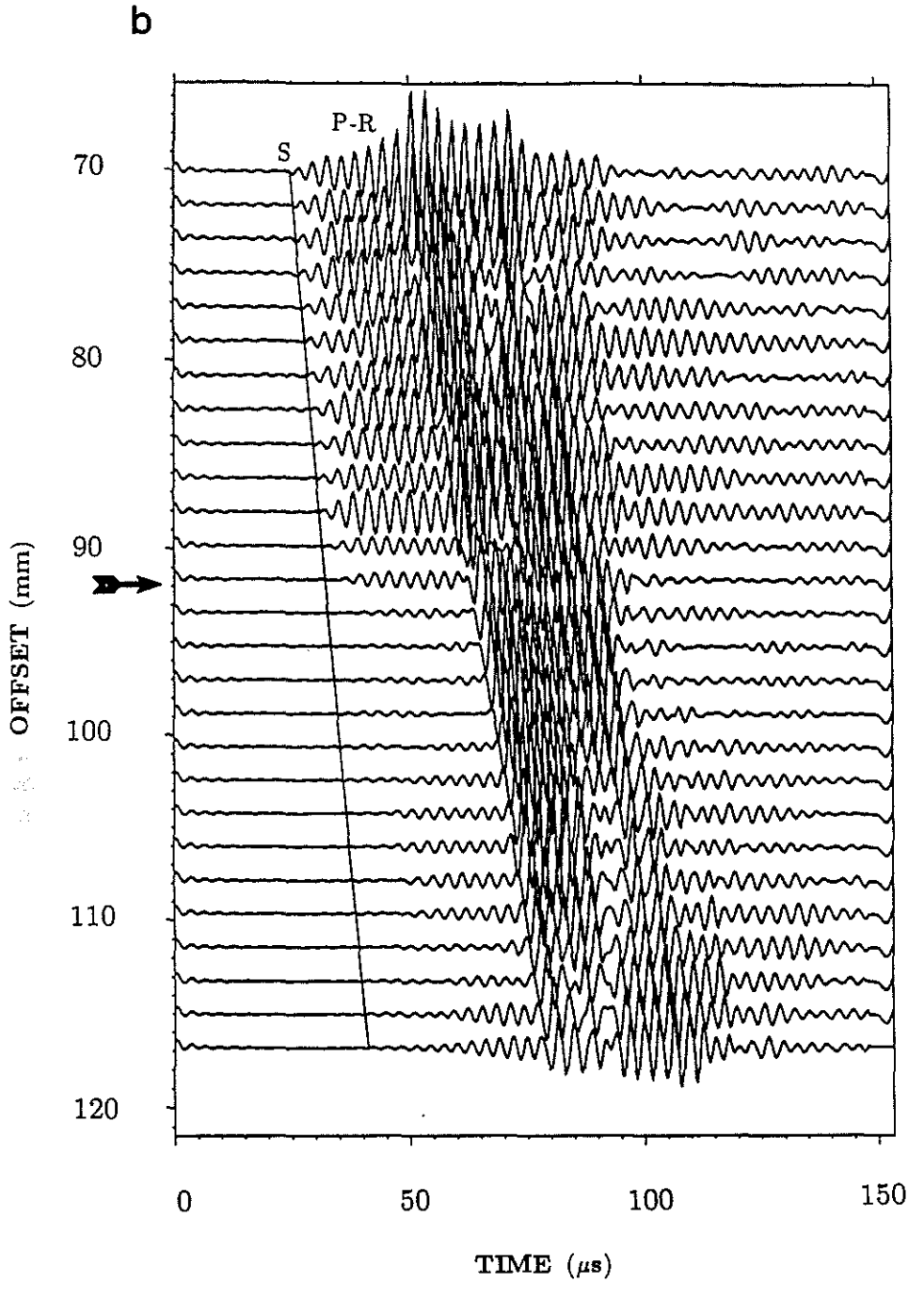
b
P-R
S
70
80
90
100
110
120
OFFSET (mm)
0
50
100
150
TIME (μs)

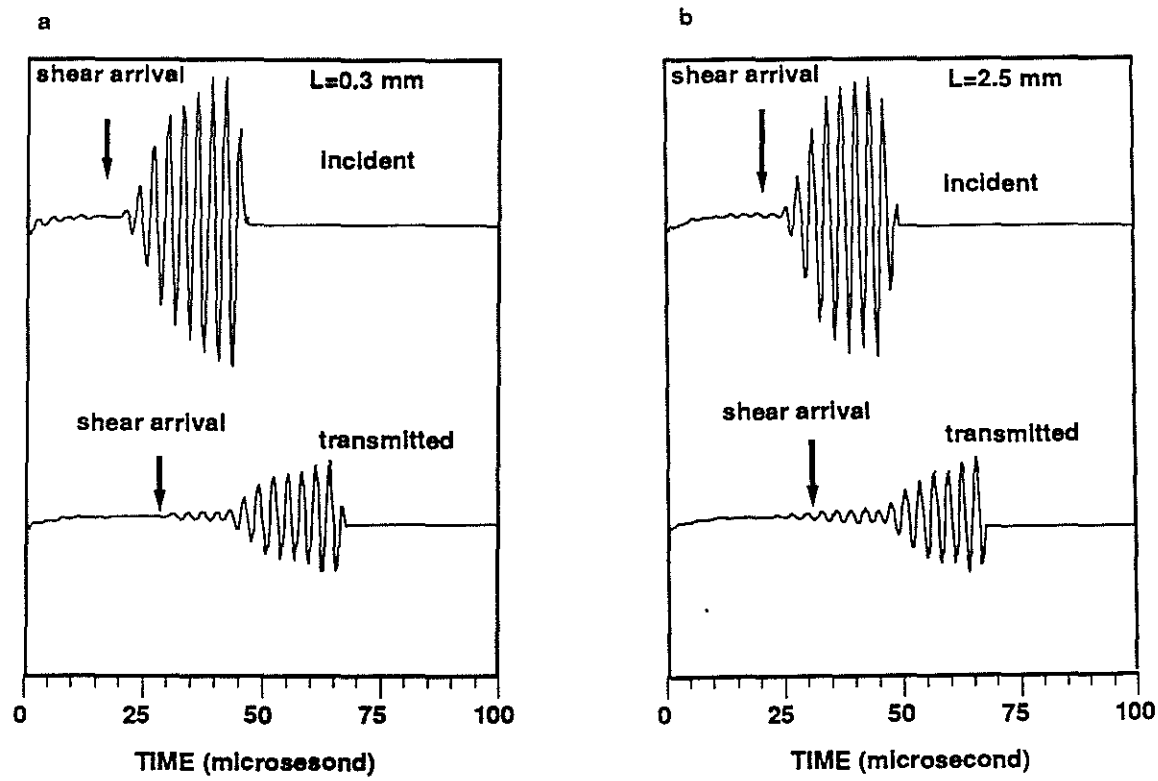

Figure 11: Averaged incident and transmitted pseudo-Rayleigh waveforms. They are obtained from the data shown in Figure 10 by windowing the signal before the fluid arrivals and stacking the traces above and below the fracture. For the transmitted waves, only the last 9 traces of (a) and (b) of Figure 10 which have coherent wave energy are used. Note the similarity between the waveforms in (a) and (b) and the weak early part of the transmitted waves.

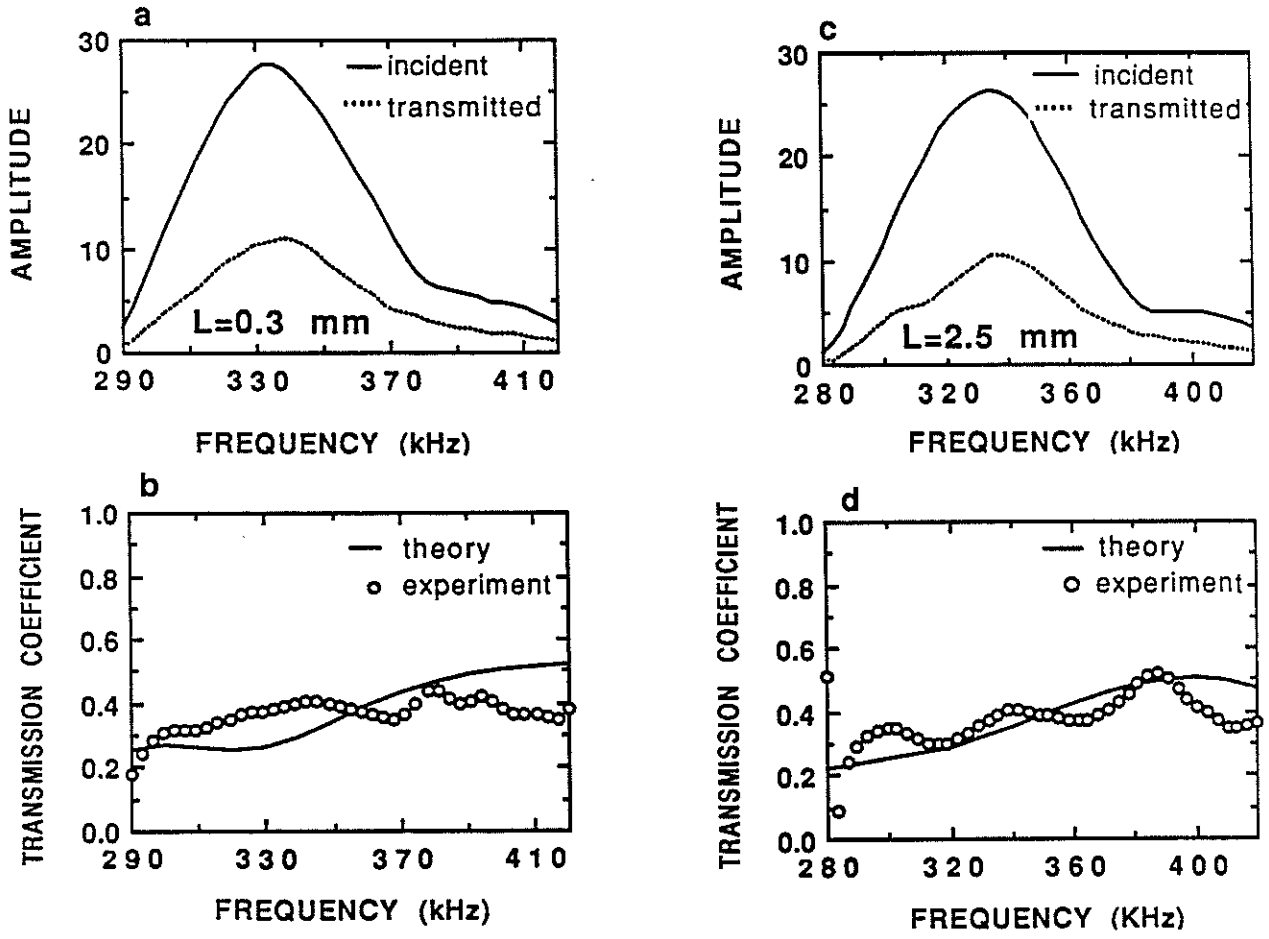

Figure 12: Experimental results obtained from the waveforms shown in Figure 11. The spectra in (a) and (c) show almost the same substantial amplitude reduction for the two very different fractures. The open circles in (b) and (d) are the measured transmission coefficients and the solid lines are the theoretical coefficients. Theory and experiment agree well.